

NASA/TP—2001–209978



Dynamic Response Assessment for the MEMS Accelerometer Under Severe Shock Loads

Mark S. Fan and Harry C. Shaw

National Aeronautics and
Space Administration

Goddard Space Flight Center
Greenbelt, Maryland 20771

October 2001

NASA/TP—2001–209978

Dynamic Response Assessment for the MEMS Accelerometer Under Severe Shock Loads

The NASA STI Program Office ... in Profile

Since its founding, NASA has been dedicated to the advancement of aeronautics and space science. The NASA Scientific and Technical Information (STI) Program Office plays a key part in helping NASA maintain this important role.

The NASA STI Program Office is operated by Langley Research Center, the lead center for NASA's scientific and technical information. The NASA STI Program Office provides access to the NASA STI Database, the largest collection of aeronautical and space science STI in the world. The Program Office is also NASA's institutional mechanism for disseminating the results of its research and development activities. These results are published by NASA in the NASA STI Report Series, which includes the following report types:

- **TECHNICAL PUBLICATION.** Reports of completed research or a major significant phase of research that present the results of NASA programs and include extensive data or theoretical analysis. Includes compilations of significant scientific and technical data and information deemed to be of continuing reference value. NASA's counterpart of peer-reviewed formal professional papers but has less stringent limitations on manuscript length and extent of graphic presentations.
- **TECHNICAL MEMORANDUM.** Scientific and technical findings that are preliminary or of specialized interest, e.g., quick release reports, working papers, and bibliographies that contain minimal annotation. Does not contain extensive analysis.
- **CONTRACTOR REPORT.** Scientific and technical findings by NASA-sponsored contractors and grantees.
- **CONFERENCE PUBLICATION.** Collected papers from scientific and technical conferences, symposia, seminars, or other meetings sponsored or cosponsored by NASA.
- **SPECIAL PUBLICATION.** Scientific, technical, or historical information from NASA programs, projects, and mission, often concerned with subjects having substantial public interest.
- **TECHNICAL TRANSLATION.** English-language translations of foreign scientific and technical material pertinent to NASA's mission.

Specialized services that complement the STI Program Office's diverse offerings include creating custom thesauri, building customized databases, organizing and publishing research results . . . even providing videos.

For more information about the NASA STI Program Office, see the following:

- Access the NASA STI Program Home Page at <http://www.sti.nasa.gov/STI-homepage.html>
- E-mail your question via the Internet to help@sti.nasa.gov
- Fax your question to the NASA Access Help Desk at (301) 621-0134
- Telephone the NASA Access Help Desk at (301) 621-0390
- Write to:
NASA Access Help Desk
NASA Center for Aerospace Information
7121 Standard Drive
Hanover, MD 21076-1320

NASA/TP—2001–209978



Dynamic Response Assessment for the MEMS Accelerometer Under Severe Shock Loads

*Mark S. Fan and Harry C. Shaw
NASA Goddard Space Flight Center, Greenbelt, Maryland*

National Aeronautics and
Space Administration

Goddard Space Flight Center
Greenbelt, Maryland 20771

October 2001

Acknowledgements

The authors would like to thank several colleagues at NASA Goddard Space Flight Center for their interest and assistance in the study of dynamic microelectromechanical systems (DMEMS) and related technologies. In particular, we thank Jeanette Plante for her constant support and encouragement during the course of this work. We also thank Ashok Sharma for interesting discussions on the accelerometer evaluation methodologies. Further, we thank Alex Teverovsky for kindly providing the SEM images for the accelerometer.

The authors are grateful to H. Weinberg (Analog Device, Inc.) for numerous conversations helping us understand the structure and function of the accelerometer, and to K. d'Souza and A. Laszloffy (Hibbitt, Karlsson & Sorensen, Inc.) for insightful discussions on the complicated numerical convergence issues relating to highly nonlinear intermittent dynamic impact simulation.

Available from:

NASA Center for AeroSpace Information
7121 Standard Drive
Hanover, MD 21076-1320
Price Code: A17

National Technical Information Service
5285 Port Royal Road
Springfield, VA 22161
Price Code: A10

TABLE OF CONTENTS

1. Introduction	1
2. Description of the Accelerometer	2
3. Finite Element Analysis (FEA) Model	3
4. Material Properties	5
5. Input Shock for the Simulation	7
6. Issues Relating to the Numerical Simulation	7
7. Numerical Results and Discussions	17
7.1 Modal Results for the System	17
7.2 Modal Results for the Sensor	19
7.3 Results of Dynamic Analysis in $\pm Z$ Axis	21
7.4 Results of Dynamic Analysis in $\pm X$ Axis	26
8. Conclusions	28
Reference	31
List of Illustrations	33

LIST OF ILLUSTRATIONS

Fig. 1	ADXL250 accelerometer device with the lid removed
Fig. 2	Overall layout of the sensor elements
Fig. 3	Enlarged view of one of the sensors
Fig. 4	Overall 3-D FEA model
Fig. 5	Enlarged device model with the lid removed
Fig. 6	Enlarged FEA model for the sensor area
Fig. 7	Details of the FEA model for the sensor
Fig. 8	Input shock
Fig. 9	Motion stopper structure
Fig. 10	Maximum principal stress at the center of the center plate (-Z shock)
Fig. 11	Maximum principal stress in the center column tether area (-Z shock)
Fig. 12	Nodal acceleration at the center of the center plate (-Z shock)
Fig. 13	Nodal acceleration in the center column tether area (-Z shock)
Fig. 14	Nodal velocity at the center of the center plate (-Z shock)
Fig. 15	Nodal velocity in the center column tether area (-Z shock)
Fig. 16	Nodal displacement at the center of the center plate (-Z shock)
Fig. 17	Nodal displacement in the center column tether area (-Z shock)
Fig. 18	Maximum principal stress at the center of the center plate (+Z shock)
Fig. 19	Maximum principal stress in the center column tether area (+Z shock)
Fig. 20	Nodal acceleration at the center of the center plate (+Z shock)
Fig. 21	Nodal acceleration in the center column tether area (+Z shock)
Fig. 22	Nodal velocity at the center of the center plate (+Z shock)
Fig. 23	Nodal velocity in the center column tether area (+Z shock)
Fig. 24	Nodal displacement at the center of the center plate (+Z shock)
Fig. 25	Nodal displacement in the center column tether area (+Z shock)
Fig. 26	Maximum principal stress at the edge of the sensor (X shock)
Fig. 27	Maximum principal stress in the center column tether area (X shock)

- Fig. 28 Maximum principal stress at the tip of the sensor finger in the center column (X shock)
- Fig. 29 Nodal acceleration at the edge of the sensor (X shock)
- Fig. 30 Nodal displacement at the edge of the sensor (X shock)

NOMENCLATURE

D_{xyz}	spatial constraints
E	Young's modulus
F	unit area force across contact interface
\mathbf{F}	external force
G	shear modulus
H	Lagrange multiplier
I	internal force matrix
J	Jacobian transformation
L	Lagrange multiplier force summation
M	mass matrix
N	interpolation function
P	external force matrix
S	surface
T_0	impact occurring moment
V	volume
$f(i), i = 1, 2, \dots$	i^{th} natural frequency
\mathbf{f}	body force, also d'Alembert force
g	gravitational constant
\mathbf{n}	surface normal vector
\mathbf{t}	surface traction vector
t	time
\mathbf{u}	displacement
\mathbf{v}	velocity

Greek Letters

Δ	differential operator
Σ	conventional summation

α	numerical damping factor
β	position dependent matrix
δ	variation operator
ϵ	strain matrix
ν	Poisson's ratio
ρ	density
σ	Cauchy stress matrix
τ	stress measure based on Jacobian transformation

Superscript

+ and –	infinitesimal time step after and before an impact
M	nodal variable
N	nodal variable
T	transposition

Subscript

A	material part coming into impact
B	material part coming into impact

DYNAMIC RESPONSE ASSESSMENT FOR THE MEMS ACCELEROMETER UNDER SEVERE SHOCK LOADS

1. INTRODUCTION

NASA Goddard Space Flight Center (GSFC) has evaluated the dynamic response of a commercial-off-the-shelf (COTS) MEMS device made by Analog Device, Inc. The device is designated as ADXL250 and is designed mainly for sensing dynamic acceleration. It is also used to measure the tilting angle of any system or component from its original level position. The device has been in commercial use (e.g., in automobile airbag deployment system as a dual-axial accelerometer and in the electronic game playstation as a tilting sensor) with success, but NASA needs an in-depth assessment of its performance under severe dynamic shock environments. It was realized while planning this evaluation task that two assessments would be beneficial to NASA's missions: 1. severe dynamic shock response under nominal thermal environments and 2. general dynamic performance under cryogenic environments. The first evaluation aims at obtaining a good understanding of its micromachined structure within a framework of brittle fracture dynamics, while the second evaluation focuses on the structure integrity under cryogenic temperature conditions. The information we gathered from the manufacturer indicated that the environmental stresses under NASA's evaluation program have been far beyond what the device has experienced with commercial applications, for which the device was designed [1]. For instance, this device has never been exposed in a thermal environment below $-40\text{ }^{\circ}\text{C}$ in the manufacturer's quality control testing. Thus NASA needs the outcome of this evaluation in order to make the selection for possible use for its missions.

This paper provides details of the first evaluation—the dynamic response under severe multi-axial single-pulse shock load. It was performed using finite element tools with nonlinear dynamics procedures.

2. DESCRIPTION OF THE ACCELEROMETER

The device is commercially available in a hermetic 14-pin surface mount cerpac package specified over the $-40\text{ }^{\circ}\text{C}$ to $+85\text{ }^{\circ}\text{C}$ temperature range. Fig. 1 shows the device with the lid removed. The silver-loaded adhesive is used to mount the chip onto the ceramic substrate.

The monolithic MEMS device was fabricated using a proprietary surface micromachining process, which combines all the signal processing circuitry on a single chip. The surface micromachined sensor elements are made by depositing polysilicon on a sacrificial oxide layer that is then etched away leaving the suspended sensor elements. Fig. 2 shows the overall layout of the surface of the chip, where two identical sensors orthogonally oriented are present to measure motions in X and Y planar directions. Fig. 3 gives a local view of one of these sensors. As can be seen, each sensor contains multiple fingers along each side of the center proof mass plate (beam). The fingers are either directly attached to the center proof mass, or to the silicon substrate (the surface of the chip) by silicon tethers which provide rigid support. The differential capacitor sensor is thus formed by fixed fingers (tether supported) and moving fingers attached to the proof mass that moves in response to acceleration along its longitudinal axis. Any movement of the proof mass causes the differential capacitance, which is then measured by the circuitry and converted into acceleration as the output. The device has the absolute maximum acceleration ratings of 500g if powered and 2000g if unpowered. Any level beyond 2000g (unpowered) is considered as loads of permanent damage.

Two major factors affect the accuracy of the acceleration measurements. As discussed above, the proper directions for sensing acceleration are along the planar orthogonal coordinates X and Y. Thus, measured accelerations off these directions (i.e., along Z-axis) are inaccurate because the Z motions do not induce differential capacitance in the fingers in the way the accelerometer is designed. In practice, the accelerometer devices are surface mounted on a PCB. Therefore, the PCB must be mounted in such a

way that the sensitive axis is along the planar directions. The second factor relates to the system resonance. When the accelerometer device is soldered onto a PCB, it becomes a part of a larger vibration system including the PCB, the fixture, the accelerometer, and the other components on the board. In reality, the PCB and the mounting fixture will deflect and deform, which could be sensed by the accelerometer and produce spurious output. If the resonant frequency of the whole structure is within the signal band, motions caused by the structure itself will be shown in the sensor output resulting in signals larger than they really are, rendering the measurement useless. The key to alleviate this problem is to have a stiff PCB mounting. Since a PCB is much stiffer in its plane than in the direction perpendicular to its plane, it is imperative to ensure the sensitive axis is along the planar directions. Other possible solutions to damp the resonance include mounting the accelerometer device near a mounting post if the PCB is relatively larger in size, and securing the PCB with added mounting fixtures to increase its stiffness.

3. FINITE ELEMENT ANALYSIS (FEA) MODEL

To simulate dual-axis dynamic response to severe shock, a FEA model was created for the whole accelerometer device surface mounted through 6.0 mil thick solder joints to a PCB board. To maintain high stiffness, the PCB dimensions are chosen to be 3.0 in \times 3.0 in \times 0.062 in, and four corners and center points between the corners along the four edges of the PCB are fixed with nuts and bolts, thereby restraining all the degree-of-freedom in the corners as well as at those four center points. Fig. 4 gives the general view of the FEA model. The model consists of 22878 8-node solid elements representing 8 different materials including bulk silicon for the chip, thin-film silicon for the micromachined sensor, ceramic material (Al_2O_3 96%) for the cerpac package, die attachment adhesive, glass seal for the ceramic lid, Kovar for the gull-wing leads, polyimide glass for the PCB, and the 63:37 eutectic solder. The whole model has the characteristic lengths ranging from about 1.0 μm to 3.0 in.

Since this FEA model was built for highly nonlinear transient dynamic analyses, the high number of degrees of freedom will inevitably take long CPU time to solve. Because of the tiny characteristic lengths (slightly above 1.0 μm) in the acceleration sensor, fine meshes (in micrometer scales) must be utilized in order to achieve reasonable accuracy. In fact, these fine meshes are also numerically necessary because of the intermittent contact (discussed below) of the fingers to their neighbors (X and Y motions), as well as to the silicon base (Z motions). Without sufficiently fine mesh density, numerical convergence is extremely hard to achieve when intermittent contacts occur in the dynamic motions responding to the pulsed shock externally applied. Obviously, for a model with characteristic lengths from micrometers to inches, finite element connectivity requires high density meshes even in the areas where the respective dynamic responses are not of main interest. To reduce the degrees of freedom in those less interested areas and to make the solving process more efficient without compromising accuracy, bilinear multi-point constraint schemes were incorporated into the model in several areas including the interface between the silicon base and the die attachment, as well as the interface between the center lead on each side and the ceramic package.

To have a better view for the device, Fig. 5 shows the inside of it with its ceramic lid removed. The details of the surface micromachined sensor are shown in Fig. 6 and Fig. 7.

Two simplifications were made when building this model. The first one is that the chip contains only one sensing area, which is the X sensor shown in Fig. 2. Since the two orthogonally oriented sensors are independent to each other in their operations, and the suspended thin-film part of each sensor is extremely light in weight, we believe that analyzing only the X sensor for its response to the shock will suffice in obtaining information about its structural integrity as the same results shall directly be applicable to the Y sensor. It was estimated that removing the Y sensor from this model reduced the total degree-of-freedom by 38%. The second simplification is for the tethers used to hold the fixed fingers down to the surface of the chip. To further reduce the degree-of-

freedom of the model, the circular-cone shaped tethers are represented by the rectangular-shaped solid elements with the identical thickness. This modification in the shape of the tether may increase the local stress concentration at the tether-finger interface, which is considered more conservative for the local stress. Before using this model for the final analysis, a dual-axis test-run was conducted under the same shock conditions to examine whether the local interfacial stresses are beyond the thin-film silicon's fracture strength. The results from the test-run indicated that the local stress concentration was still in the safe region. Other than the local interfacial areas, this simplification should have no impact on the dynamic response to the shock applied. We also learned from the manufacturer that the tethers were designed for providing relatively rigid support to the fingers without much flexibility. Therefore, this simplification should be justifiable.

4. MATERIAL PROPERTIES

Because the analysis is to be conducted under the normal room temperature, linear properties are used in the simulation. Thus, in this simulation the nonlinearities are from two sources, i.e., geometric nonlinearities and intermittent contact nonlinearities. Table 1 summarizes those property values for the FEA.

The fracture strength of the thin-film silicon needs to be explained, as it is one of the most critical data to be used for structural integrity assessment for this MEMS device. Thin-film silicon includes varying thickness of silicon "sheets", but the terminology is usually for micro-sized silicon features micromachined on single-crystalline silicon wafers that have thickness typically under 20 μm . Studies for the elastic fracture of thin-film silicon under deforming loads have been popular recently because of rapid development in the MEMS technologies [2, 3, 4, 5 & 6]. Unlike the bulk silicon which is generally treated as isotropic material, the thin-film silicon in the micrometer scales displays high directional preferences in its structural properties. Thus, obtaining accurate properties for the thin-film material is the key to accurate results.

Table 1

Materials	Young's Modulus (GPa)	Poisson's Ratio	Mass Density (kg/m ³)	Fracture Strength (GPa)
Si (bulk)	161	0.28	2330	-
Si (film)	E ₁₁₀ =161 E ₁₀₀ =130 G ₁₁₀ =80 G ₁₀₀ =50	ν_{110} =0.279 ν_{100} =0.064	2330	Low: 0.6 Avg: 1.0-3.0
Al ₂ O ₃ 96%	303	0.21	3720	-
Adhesive	3.5	0.33	1200	-
Glass Seal	56.6	0.27	2750	-
Kovar	138	0.31	8360	-
Polyimide	21	0.33	2214	-
Solder	14.9	0.29	8470	-

Most measurements for the fracture strength were conducted by applying a static load to a micro-sized cantilever beam micromachined from the thin wafer. These experiments were well controlled and monitored *in situ* inside a scanning electron microscope. Studies have found that the fracture strength is sensitive to the surface roughness and natural flaws, thus the data obtained were within a scattered band. Attempts were made to polish the Si surfaces by applying diamond paste (typically 1-3 μm) to increase the fracture strength, but the fracture strength actually decreased by a fairly large percentage. Later, it was found that a diamond polishing followed by thermal oxidization could not only restore the original strength, but also slightly increase it. The data listed in Table 1 are mainly from measurements that are not polished and oxidized because the expensive treatment for the Si surface resulted only a 15-20% increase in fracture strength compared to untreated Si. The lowest strength reported is 0.6 GPa, while the high end goes slightly above 3.0 GPa. As a conservative assessment, we will use 0.6 GPa as our fracture criterion.

5. INPUT SHOCK FOR THE SIMULATION

The numerical analyses simulate a severe pulsed shock applied to the MEMS device with a magnitude being equal to the maximum unpowered acceleration rating (2000g). The duration of the shock is only 0.01 seconds. This input shock profile is plotted in Fig. 8, and is applied in the analyses to both X (planar) and Z (vertical) directions. As has been mentioned, this dual-axis accelerometer is designed to withstand and sense the accelerations in the X and Y (planar) directions, and the Z acceleration measurement will generate spurious readings. For the most popular applications such as automobile air bag release systems, ensuring the acceleration in only the planar directions is not hard to arrange, but this is perhaps impossible for a spacecraft being launched or in its orbit. Thus vertical shock in Z is also carefully analyzed and examined to ensure structural integrity when the shock occurs along non-planar directions.

6. ISSUES RELATING TO THE NUMERICAL SIMULATION

ABAQUS/Standard is the FEA code used for this simulation. For highly nonlinear dynamic analysis of a system under severe shock, a common FEA procedure is to perform direct time domain integration for all of the degrees of freedom in the model. Two numerical methods are available to conduct the numerical analysis, namely, explicit and implicit integration. In our case, the explicit scheme shall provide a more efficient solution if the upper bound time increment Δt is well controlled to avoid instability problem. Unfortunately, we do not have ABAQUS/Explicit code available at this time. ABAQUS/Standard uses the implicit scheme with the Hilber-Hughes-Taylor operator and the iteration is performed through Newton's method [7]. For linear systems, the Hilber-Hughes-Taylor operator provides guaranteed numerical stability because the upper bound of the time increment is theoretically unlimited. In extreme cases where the system is highly nonlinear, obtaining a stable solution may be difficult with the implicit scheme. However, nonlinearities are generally more accounted for in dynamic systems than in

static systems since the inertia terms in the nonlinear governing equations provide theoretical stability to the system. Therefore, the implicit operator is generally very effective in dealing with most nonlinear dynamic solutions except very few extreme cases. Implicit integration scheme shall give accurate results in most structural problems if the set time increments are no more than one order of magnitude of the stability limit of the explicit scheme, but the accuracy deteriorates in the dynamic response prediction as the time increment increases to a point where it is comparable to the period of typical modes of response. To achieve good results utilizing the implicit scheme, time increments must be closely monitored and controlled using the “half-step residual” criterion [8]. While there is no technical difficulty in doing so, it is very much CPU intensive and therefore the analysis could be very expensive compared to the explicit integration. Nevertheless, explicit scheme in certain cases could also be very expensive because a conditionally stable integration operator can result in extremely small time steps in order to achieve stability, therefore, taking much longer to obtain a converged solution.

An inexpensive alternative to direct integration scheme (especially to the implicit scheme) is to invoke the transient modal dynamic procedure for many dynamic problems. This procedure gives the response of the model as a function of time based on a given time-dependent loading. Since the dynamic response of the structure is based on a subset of the eigenmodes of the system, sufficient number of eigenmodes must be extracted before commencing the transient modal dynamic analysis. In this analysis, the modal amplitudes are integrated through time, and the system response is synthesized from the modal responses. Transient modal dynamic analysis is a linear perturbation procedure, and will not give accurate results for problems with nonlinear load inputs. However, the procedure is very accurate if the load amplitude curve is discretized in such a way that the magnitude of the excitation varies linearly within each discretized segment. The proper discretization of the load input is critical to achieve good results. Nevertheless, we were not able to take the advantage of the modal dynamic analysis, as the model contains multiple contact surfaces that render the linear perturbation procedure completely useless. The contact issue will be discussed below.

Another alternative, which can handle nonlinear problems and is less expensive than the nonlinear direct integration, is the so called subspace dynamic analysis using “subspace projection” method. It performs direct explicit integration of the dynamic equations expressed in terms of a vector space spanned by a number of eigenvectors. In this method, eigenmodes must be extracted first before performing dynamic analysis. This alternative to the direct integration scheme is highly effective and efficient for solving problems with mild nonlinearities that do not substantially change the eigenmodes. Unfortunately, just like the transient modal dynamic analysis, the subspace projection is not useful when contacts present in the model because of the highly nonlinear nature of contacts. Given the fact that ABAQUS/Standard is the only tool available, the problem being dealt with in this paper must be solved using the most expensive approach, i.e., direct integration of all the nonlinear equations with the Hilber-Hughes-Taylor integration operator.

To derive the equations for the nonlinear dynamics, we begin with the classic form of the virtual work equation:

$$\int_V \boldsymbol{\sigma} : \delta \boldsymbol{\varepsilon} dV = \int_S \delta \mathbf{v} \cdot \mathbf{t} dS + \int_V \delta \mathbf{v} \cdot \mathbf{f} dV \quad (6.1)$$

where $\boldsymbol{\sigma}$ is the Cauchy stress matrix, $\delta \boldsymbol{\varepsilon} = \frac{1}{2} \left(\frac{\partial \delta \mathbf{v}}{\partial \mathbf{x}} + \left[\frac{\partial \delta \mathbf{v}}{\partial \mathbf{x}} \right]^T \right)$ is the virtual variation of the strain matrix, $\mathbf{t} = \mathbf{n} \cdot \boldsymbol{\sigma}$ is the surface traction vector, and \mathbf{f} is the body force.

According to the concept of work conjugacy, we have:

$$\boldsymbol{\tau} = J \boldsymbol{\sigma} \quad (6.2)$$

where $\boldsymbol{\tau}$ is the stress measure equivalent to work conjugate to the strain measure, and J is the Jacobian of the elastic deformation defined as $J = dV/dV_0$. Substituting Eq. (6.2) into Eq. (6.1) yields:

$$\int_{V_0} \boldsymbol{\tau} : \delta \boldsymbol{\varepsilon} dV_0 = \int_S \delta \mathbf{v} \cdot \mathbf{t} dS + \int_V \delta \mathbf{v} \cdot \mathbf{f} dV \quad (6.3)$$

The finite element interpolator can be written as:

$$\mathbf{u} = \mathbf{N}^N u^N \quad (6.4)$$

Hence

$$\frac{\partial^2 \mathbf{u}}{\partial t^2} = \mathbf{N}^N \frac{\partial^2 u^N}{\partial t^2} \quad (6.5)$$

where \mathbf{N}^N is the interpolation function that is not displacement dependent [9], and u^N is the nodal variable. Here the summation convention is adopted for the superscripts.

The virtual field in the Eq. 6.2, $\delta \mathbf{v}$, needs to be compatible with all kinematic constraints, thus:

$$\delta \mathbf{v} = \mathbf{N}^M \delta v^M \quad (6.6)$$

In Eq. 6.3, $\delta \boldsymbol{\varepsilon}$ is the virtual rate of strain associated with $\delta \mathbf{v}$, and because it is a rate form, it must be linear in $\delta \mathbf{v}$. Thus, the interpolation assumption leads to:

$$\delta \boldsymbol{\varepsilon} = \boldsymbol{\beta}^N \delta v^N \quad (6.7)$$

where $\boldsymbol{\beta}^N$ is a matrix generally depending on the current position \mathbf{x} of the material.

Hence Eq. (6.3) becomes:

$$\int_{V_0} \boldsymbol{\tau} : \boldsymbol{\beta}^N dV_0 = \int_S \mathbf{N}^N \cdot \mathbf{t} dS + \int_V \mathbf{N}^N \cdot \mathbf{f} dV \quad (6.8)$$

Now we write out the d'Alembert force in the equilibrium state:

$$\mathbf{f} = \mathbf{F} - \rho \frac{\partial^2 \mathbf{u}}{\partial t^2} \quad (6.9)$$

where \mathbf{F} is an externally prescribed force. The virtual work equation in terms of the body force is:

$$\int_V \mathbf{f} \cdot \delta \mathbf{v} dV = \int_V \mathbf{F} \cdot \delta \mathbf{v} dV - \int_V \rho \frac{\partial^2 \mathbf{u}}{\partial t^2} \cdot \delta \mathbf{v} dV \quad (6.10)$$

Based on the d'Alembert principle, the last term in Eq. 6.10 can be written as:

$$- \int_{V_0} \rho_0 \frac{\partial^2 \mathbf{u}}{\partial t^2} \cdot \delta \mathbf{v} dV_0$$

where ρ_0 is the reference density. Using the interpolation relations, we can rewrite this term as:

$$- \left(\int_{V_0} \rho_0 \mathbf{N}^N \cdot \mathbf{N}^M dV_0 \right) \frac{\partial^2 u^M}{\partial t^2}$$

Hence Eq. (6.8) can be expressed as:

$$M^{NM} \frac{\partial^2 u^M}{\partial t^2} + I^N - P^N = 0 \quad (6.11)$$

where

$$M^{NM} = \int_{V_0} \rho_0 \mathbf{N}^N \cdot \mathbf{N}^M dV_0$$

is the mass matrix;

$$I^N = \int_{V_0} \boldsymbol{\tau} : \boldsymbol{\beta}^N dV_0$$

is the internal force vector, and

$$P^N = \int_S \mathbf{N}^N \cdot \mathbf{t} dS + \int_V \mathbf{N}^N \cdot \mathbf{F} dV$$

is the external force vector.

Eq. (6.11) is the finite element form of the equilibrium equation. The nonlinear integration operator defined by Hilber, Hughes and Taylor is based on Eq. (6.11) and has a more complex form:

$$M^{NM} \frac{\partial^2 u^M}{\partial t^2} \Big|_{t+\Delta t} + (1 + \alpha)(I^N \Big|_{t+\Delta t} - P^N \Big|_{t+\Delta t}) - \alpha(I^N \Big|_t - P^N \Big|_t) + L^N \Big|_{t+\Delta t} = 0 \quad (6.12)$$

where L^N is the sum of all Lagrange multiplier forces associated with degree of freedom N . This operator is completed by the following two formulae for displacement and velocity:

$$u \Big|_{t+\Delta t} = u \Big|_t + \Delta t \frac{\partial u}{\partial t} \Big|_t + \Delta t^2 \left\{ \left[\frac{1}{2} - \frac{1}{4}(1 - \alpha)^2 \right] \frac{\partial^2 u}{\partial t^2} \Big|_t + \frac{1}{4}(1 - \alpha)^2 \frac{\partial^2 u}{\partial t^2} \Big|_{t+\Delta t} \right\} \quad (6.13)$$

and

$$\frac{\partial u}{\partial t} \Big|_{t+\Delta t} = \frac{\partial u}{\partial t} \Big|_t + \Delta t \left[\left(\alpha + \frac{1}{2} \right) \frac{\partial^2 u}{\partial t^2} \Big|_t + \left(\frac{1}{2} - \alpha \right) \frac{\partial^2 u}{\partial t^2} \Big|_{t+\Delta t} \right] \quad (6.14)$$

where $0 \geq \alpha \geq -1/3$.

Eq. 6.12, 6.13, and 6.14 are directly integrated for this nonlinear dynamic analysis presented here. A salient feature of this set of equations is the built-in controllable numerical damping. This pure numerical damping is valuable in removing nonlinear iterative noise inevitably induced by time step changes. As suggested, $\alpha = -0.05$ is considered as a good choice for providing proper amounts of damping to control the nonlinear numerical noise.

Because there are no inelastic materials in the MEMS device, Rayleigh damping is utilized to simulate the dynamic response more realistically. Essentially, Rayleigh damping contains two damping factors, one for mass proportional damping and another for stiffness (strain-rate) proportional damping. The first damping is due to the material movements through a viscous “ether”, thus such an energy dissipation mechanism does not practically exist in the accelerometer despite the presence of air. The strain rate proportional damping always exists even though the materials themselves do not have plastic behavior in this device.

The most challenging issue in this simulation is the intermittent contact and impact. When the shock is applied to the device and the sensor is responding to the excitement, the fingers will have large oscillating displacements around their neutral (undeformed) positions. The amplitudes of the displacements decrease fairly rapidly due to both damping and the intermittent contacts. When the shock is along the Z axis, the intermittent contacts are one-sided, i.e., the fingers have intermittent contacts to the silicon base when moving downward and no contacts when moving upward. In the FEA model, the surface of the silicon base is categorized as rigid, and the bottom surfaces of the fingers as deformable. If the shock is applied along the X direction, the fingers will

experience two-sided intermittent contacts to their left and right neighbors. Under this scenario, the fingers' contacting surfaces are all deformable surfaces in the model. For a successful simulation of intermittent contacts, it is imperative that meshes on master surfaces and slave surfaces are sufficiently fine and are matching. This criterion was followed in building the model.

Two methods are commonly adopted to simulate contact impact phenomenon. The first method, which treats the impact as totally elastic and keeps the total kinetic energy unchanged, is mathematically simpler. The procedure is using the standard implicit integration. This method is suitable for dynamic analysis where the contact impact is less critical and the detailed stress behavior in the contact region is of little importance. However, for truly high velocity impact cases, this method may lead to excessive contact chattering and cause convergence problem. Thus the second method must be utilized in cases where the process of impact and the behavior of local stresses are critical. When using this method to simulate hard surface intermittent contact, a "local fully plastic impact" theory is adopted. This theory assumes that the total momentum of the contacting bodies remains unchanged while the nodes that are contacting will acquire the same velocity instantaneously in the direction of impact. The sudden changes in velocity and acceleration due to high-speed impact are incorporated into the simulation by developing a set of impulse equations that are solved together with the dynamics equations.

To satisfy the "local fully plastic impact" requirements, velocity and acceleration in the impact interface region at the time of impact shall be governed by these relations:

$$\mathbf{n} \cdot \frac{\partial \mathbf{u}_A}{\partial t} = \mathbf{n} \cdot \frac{\partial \mathbf{u}_B}{\partial t} \quad (6.15)$$

$$\mathbf{n} \cdot \frac{\partial^2 \mathbf{u}_A}{\partial t^2} = \mathbf{n} \cdot \frac{\partial^2 \mathbf{u}_B}{\partial t^2} \quad (6.16)$$

where A and B denote part A and part B coming into impact, and \mathbf{n} is the local normal to the contact interface.

Due to contact impact, the interfacial velocity jumps suddenly, which can be expressed as:

$$\Delta\left(\frac{\partial \mathbf{u}}{\partial t}\right) = \left(\frac{\partial \mathbf{u}}{\partial t}\right)^+ - \left(\frac{\partial \mathbf{u}}{\partial t}\right)^- \quad (6.17)$$

where the superscripts $+$ and $-$ denote infinitesimal time steps after and before an impact respectively. Thus, Eq. 6.15 becomes:

$$\mathbf{n} \cdot \left[\Delta\left(\frac{\partial \mathbf{u}_A}{\partial t}\right) + \left(\frac{\partial \mathbf{u}_A}{\partial t}\right)^- \right] = \mathbf{n} \cdot \left[\Delta\left(\frac{\partial \mathbf{u}_B}{\partial t}\right) + \left(\frac{\partial \mathbf{u}_B}{\partial t}\right)^- \right] \quad (6.18)$$

Let F be the force per unit area across the interface along \mathbf{n} , and let T_0 be the moment when the impact occurred, then the following relations hold:

$$F_A = -F_B \quad (t \geq T_0) \quad (6.19a)$$

$$F_A = F_B = 0 \quad (t < T_0) \quad (6.19b)$$

where F includes all forces in the contact interface along \mathbf{n} except for d'Alembert forces. Thus the virtual work equation during the impact is:

$$\sum_{A,B} \left(\int_V \rho \frac{\partial^2 \mathbf{u}}{\partial t^2} \cdot \delta \mathbf{u} \, dV \right) + \int_S (F_A \mathbf{n} \cdot \delta \mathbf{u}_A + F_B \mathbf{n} \cdot \delta \mathbf{u}_B) dS = 0 \quad (6.20)$$

Integrating Eq. (6.20) from T_0^- to T_0^+ (time duration of velocity jump) yields:

$$\sum_{A,B} \left(\int_V \rho \frac{\partial^2 \mathbf{u}}{\partial t^2} \cdot \delta \mathbf{u} dV dT \right) + \int_S \int_T (F_A \mathbf{n} \cdot \delta \mathbf{u}_A + F_B \mathbf{n} \cdot \delta \mathbf{u}_B) dS dT = 0 \quad (6.21)$$

In view of Eq. (6.15) and (6.19a), the second term in Eq. (6.21) is zero. However, the constraint (Eq. 6.18) needs to be satisfied for simulating the process of contact impact. Eq. (6.21) is then augmented with a Lagrange multiplier term, with H being the multiplier. After taking the variation calculations, we obtain:

$$\begin{aligned} & \sum_{A,B} \left[\int_V \rho \Delta \left(\frac{\partial \mathbf{u}}{\partial t} \right) \cdot \delta \mathbf{u} dV \right] + \int_S H \mathbf{n} \cdot (\delta \mathbf{u}_A - \delta \mathbf{u}_B) dS \\ & + \int_S \left[\Delta \left(\frac{\partial \mathbf{u}_A}{\partial t} \right) - \Delta \left(\frac{\partial \mathbf{u}_B}{\partial t} \right) \right] \cdot \mathbf{n} \delta H dS \\ & + \int_S \left[\left(\frac{\partial \mathbf{u}_A}{\partial t} \right)^- - \left(\frac{\partial \mathbf{u}_B}{\partial t} \right)^- \right] \cdot \mathbf{n} \delta H dS = 0 \end{aligned} \quad (6.22)$$

Eq. (6.22) is the impulse equation, which must be solved for velocity jump at the time of contact impact.

In fact, the Lagrange multiplier H represents the pressure across the contact interface, so monitoring the H value provides a good indication for separation of the two contacting surfaces. For this sensor configuration, separation occurs immediately after impact. In the numerical simulation, impact and separation are assumed to occur at an intermediate point in a time step. The numerical scheme first solves the time step by ignoring impact, then calculates the average time of impact or separation of all the points changed inside the increment, and again solves the increment to that time interval.

7. NUMERICAL RESULTS AND DISCUSSIONS

7.1 Modal Results for the System

Modal analysis was first conducted to obtain the resonant frequencies of the system. As discussed earlier, the modal studies are important in guiding the mounting scheme of the device so that no spurious signals will be generated due to system resonance to ensure accuracy of measurements.

No particular difficulty arises in mounting the device as long as the resonant frequencies are assured to be above the frequency band of interest. For this accelerometer device, the typically rated bandwidth is 1.0 kHz [1]. The vendor has suggested a number of mounting ways in their literature to achieve higher system resonance [10]. Based on vendor's testing results, soldering the device onto a PCB with conformal coating yields a fundamental resonance of 12 kHz [1]. Thus it is well above the frequency band of interest. It seems that mounting the device with standard surface mount onto any PCB would satisfy the requirements for good measurement. However, care must be taken in interpreting and using the testing data when preparing for the acceleration measurement. The testing result of 12 kHz is the fundamental resonance of the device itself, i.e., the whole MEMS device with its ceramic package is the only vibrational mass supported by the 14 metal leads. In practice, the device is only a part (perhaps a very small part) of a large vibrational mass when it is attached to a PCB that is also mounted inside an electronic box containing several PCBs and numerous active and passive devices. The contribution to the spurious output could be from sources other than the device itself even if the fundamental resonance of the device satisfies the above requirement for the frequency band. Thus, we must look into the whole system (or a subsystem, if deemed proper) when determining whether there are possible interferences with the actual readings of the sensor. A simple example can well explain this point. Performing a procedure of linear perturbation eigenmode extraction using our FEA model, we obtained the following results summarized in Table 2:

Table 2

Cases	PCB locations of Restraint $D_x = D_y = D_z = 0$	Fundamental PCB Resonance (Hz)
1	4 corners	312
2	4 corner plus 4 center points between corners on the edges	398
3	2 opposite edges	488
4	4 edges	541
5	4 edges plus PCB center point	1325

The above results illustrate how sensitive the resonance could be when a dynamic system changes its boundary conditions. Attaching a subsystem to a larger dynamic system is essentially equivalent to changing the boundary conditions of the subsystem, although it is not always straightforward to modify the subsystem's boundary conditions to represent an equivalent larger system. If modifying the boundary conditions cannot obtain an equivalent larger system, then simulation must include all the elements contained in the larger system in order to get reasonable results. For each of the 5 cases listed in Table 2, the eigenmode procedure extracted first 6 resonant frequencies ranging from several hundred Hz to several thousand Hz. Examining these modal shapes revealed that none of the modes has pure planar motions, indicating that modes with pure planar motions shall have even higher frequencies (well above 1.0 kHz, which is the bandwidth for this device). Thus, when the direction of acceleration is known, and the PCB is mounted so that the sensing direction is in its planar orientations, this device shall give minimum spurious output. However, when the larger system is complicated, determining the correct orientation of the mounting is not always easy. A great deal of effort must be devoted to the study of this issue before the actual measurements start.

7.2 Modal Results for the Sensor

An interesting issue relating to modal analysis is the natural frequency for the sensor itself. Essentially, the sensor includes the proof mass plate, the sensor fingers attached to the center plate, the force fingers attached to the silicon base, and the tethers attaching force fingers. The manufacturer has tested its fundamental resonance, which is 24 kHz [1]. The method used to obtain this frequency is to statically displace the center proof mass along its longitudinal coordinate (X coordinate in the FEA model) by a microprobe, and release it to induce free vibration. The amplitudes of this vibration decrease largely due to the strain-rate proportional damping, which is represented by the second component of Rayleigh damping mechanism. By monitoring the vibration spectra in a frequency domain, a small peak at 24 kHz was observed.

An independent eigenmode extraction procedure was performed to obtain the resonant frequencies for the sensor alone. In this analysis, the bottom of each tether is modeled as rigid attachment to the silicon base, which is essentially the same as the function of tethers in the microprobe-induced free vibration testing. The results are as follows:

$$f(1) = 18.7 \text{ kHz}$$

$$f(2) = 32.5 \text{ kHz}$$

$$f(3) = 43.1 \text{ kHz}$$

$$f(4) = 46.8 \text{ kHz}$$

$$f(5) = 78.1 \text{ kHz}$$

$$f(6) = 90.2 \text{ kHz}$$

Among these resonant frequencies, only $f(3)$ is a pure planar mode moving strictly along the X-axis. Other frequencies have significant Z components in their modes and are not comparable to the microprobe measurement. Obviously, $f(3)$ is much higher than 24 kHz from measurement. To further investigate this discrepancy and to verify the results from the first eigenmode analysis, another eigenmode extraction

procedure was conducted for the purpose of searching for any existing eigenmodes within the frequency band between 20 kHz and 30 kHz using the Lanczos algorithm. None were found within that frequency band. An expanded Lanczos procedure produced the identical results listed above. So we concluded that $f(3)$ should be the mode that was induced by the microprobe experiment.

Now we need to explain the large discrepancy between the experiment and the simulation. For the induced free vibration with viscous effect of air being negligible, our experience pointed out that the fundamental resonance from both experiment and analysis should be very close. A 15% discrepancy would indicate a problem. After a careful examination of the free vibrational motions along the X-axis, we gained a good understanding of the issue. In eigenmode extraction analysis, the procedure is a linear perturbation and all the contact surfaces are ignored in carrying out the simulation. Thus the center plate is allowed to move freely along the X-axis. However, the sensor was designed to have two “motion stoppers”, one on each side of the center plate along the X-axis (Fig. 9). These stoppers are rigidly tethered down to the silicon base and confine the center plate movements along the X-axis within about 1.2 μm from its undeformed position (1.2 μm being the gap between the end of the center plate and the head of the stopper). When the center plate is displaced along the X-axis by the microprobe during the frequency experiment, the maximum distance it could statically travel is no more than 1.2 μm . Two things could be discussed here: firstly, because the initial amplitudes and the system potential energy are extremely small, the measurement apparatus may not have sufficient resolution to pick up the higher frequency modes which generally require higher kinetic energy to get excited. Secondly, even if the initial potential energy is sufficient to excite higher modes after the center plate is released by the microprobe, the impacts between the plate and the stoppers quickly consume the kinetic energy of the plate. Thus the underlying physics of the oscillating motion under the second scenario is quite different from that of linear perturbation motion.

Based on our observation and the way the sensor resonance was measured, we believe that the theoretical resonant frequency for the pure planar mode should be higher

than 24 kHz. Because of the presence of multiple contact surfaces, the theoretical resonance should not be compared directly with the experimental result (24 kHz). The measured resonance is perhaps due to complicated secondary effect of the dynamic system, and is likely measurement-technique dependent.

7.3 Results of Dynamic Analysis in $\pm Z$ Axis

As has been discussed earlier, the Z-axis is not a sensing orientation by design and the mounting scheme should make the X-axis (or Y-axis because of the dual-axis capabilities) be the direction of measurement. However, it is inevitable for the device to experience shocks along the Z-axis during space flight, though this is practically not a concern for most commercial applications. For space flight applications, study of shock impact in the Z-axis is as important as in other axes to ensure that the sensor can withstand severe dynamic conditions.

The impact mechanism in the Z-axis shock is different from that in the X- or Y-axis shocks. In the Z-axis, the major potential damaging mechanism is the contact impact between the fingers and the silicon base. Intuitively this impact is severer than that in the X-axis shock for the fingers, as in the X-axis both the sensor fingers and the force fingers move in the same direction [11] in response to the shock applied, making all the contact surfaces deformable. In the case of Z shock however, the surface of the silicon chip does not deform (rigid surface) during the impact, and the dynamic stresses in the center plate and in the fingers are expected to be higher. This is the stress on which the analysis is focused.

Several areas in the sensor are of key interest for local stress evaluation. For the Z impact, the geometric center of the center plate and the tether area of the force fingers in the center column are expected to have high stress concentrations. In the case of X impact, the interest of the stress in the center column fingers remains the same, but the center of the center plate is no longer a critical area because no contact will occur in that

area. Instead, the critical area to be examined is at the edge of the center plate where it will have intermittent contact with the stopper. To obtain better stress results, these areas of interest are analyzed with locally refined meshes.

Unlike motions along the X-axis where +X or -X shock produces nearly identical dynamic results due to nearly symmetric geometry of the sensor, shocks applied to +Z and -Z directions will produce highly different results. When the shock is applied along the -Z-axis (pointing downward), the initial motion of the center plate is upward with no contact to the silicon base. The plate then moves downward after the end of the shock duration, having the first contact to the base, then moves up again with the contact surfaces separated. This cycle of oscillating motion repeats many times with a decreasing amplitude due to the intrinsic damping. If the shock is along +Z however, the initial center plate movement goes downward, making instant contact to the base. Then the contact surfaces separate and the plate moves upward. This pattern of motion also repeats many times till all the kinetic energy is completely consumed. Obviously, the +Z shock should result in higher dynamic stresses in the sensor because the initial impact of the contact surfaces is severer.

Let us first examine the -Z shock in greater detail. Fig. 10 depicts the time history of the maximum principal stress at the center point of the center plate. As expected, the response starts at 0.01 sec at which the shock (Fig. 8) is applied. Since the shock is in the direction of -Z, the initial movement of the center plate and the fingers is upward (+Z). The highest maximum principal stress induced is about 4.8 MPa, which occurs at the moment the shock is applied (at 0.01 sec). As seen in Fig. 8, the shock has a duration of 0.01 sec with a constant value of 2000g. Within the duration of the shock, the maximum principal stress is kept in a positive level with a maximum range from 2.0 MPa to 4.8 MPa. This maximum stress range decreases fairly rapidly to a smaller range from roughly 2.5 MPa to 3.6 MPa within 0.01 sec of time due to the damping effect. That positive level of stress within the 0.01 sec duration of the input shock indicates that no contacts occurred between the sensor and the silicon base before 0.02 sec of total time elapsed. This is because, for the contact to occur, the sensor must move down (after the

initial upward peaks) towards the silicon base passing through its neutral position (i.e., undeformed position), and the maximum principal stress at the sensor's neutral position must be zero.

If there were no silicon base underneath the sensor, the downward amplitude of the center plate would be quite comparable to the upward amplitude starting from 0.02 sec when the input shock ends. However, the presence of the silicon base prevents the sensor plate from moving downward for more than $2\ \mu\text{m}$ (the thickness of the tether). Thus, despite the dynamic impact from the contacts, the compressive maximum principal stress is very low due to the physical restraint of the sensor structure. This is well reflected in Fig. 10 after 0.02 sec of total time elapsed. It is also seen that, due to the intrinsic damping, the stress decreases to virtually zero at somewhere between 0.15 and 0.2 sec of the total time. This indicates that the thin-film sensor structure is indeed very stiff, taking only a fraction of a second to return to the neutral position.

Another area of interest from the stress standpoint is the tether area of the force finger in the center column. This area is found to have the highest dynamic stresses in the whole sensor structure being subject to the $-Z$ shock. The time history of the maximum principal stress is shown in Fig. 11 where the highest stress at the time of shock application is found to be 68 MPa. The stress behavior within the duration of the shock is very similar to the case plotted in Fig. 10. Interestingly, the oscillating stress after 0.02 sec time elapse is only in the positive side, indicating non-existence of compressive stress. This must be true as the area reflected in Fig. 11 is in close proximity to the tether of the force finger in the center column, and the tether structure prevents any downward movement that results in the compressive stress. Thus, there is no intermittent contact in this case.

Time history of nodal acceleration is also computed corresponding to the above cases. Figs. 12 and 13 show the nodal acceleration at the geometric center of the sensor and near the tether of the center column respectively. The behavior of these acceleration curves is well expected under the $-Z$ shock. The peak acceleration at 0.01 sec is higher

near the tether compared to that at the geometric center. For the area near the tether, the peak acceleration is as high as 26670 m/s^2 . For extremely tiny and light structure being subject to a shock of this magnitude, this huge acceleration is no surprise.

Nodal velocity plots for the geometric center as well as the tether area with the highest stress are presented in Figs. 14 and 15 where both velocity plots display very similar behavior. As expected from their acceleration comparison, the peak velocity near the tether (1549 m/s) is higher than that at the center of the sensor.

The last variable of interest in these two locations is the nodal displacement. Figs. 16 and 17 plot the displacements at the plate center and near the tether respectively. In Fig. 16, one can see that the maximum upward displacement at the center of the plate within the duration of the shock is about 2.6 mil (66 μm). During the time period of intermittent contacts between the sensor and the silicon base (a small fraction of a second starting from 0.02 sec), the maximum downward displacement is about 0.09 mil. In reality, the sensor's center point can move no more than 2 μm (0.08 mil) downward. Similarly, Fig. 17 reveals a maximum upward displacement of 0.8 mil and a downward displacement of 0.05 mil. This is obviously due to the motion restriction from the rigid tether structure.

The results from the analysis with a +Z shock input are, as expected, quite different. We shall examine the +Z results in the same order as in the -Z case. Fig. 18 depicts the maximum principal stress at the sensor's center. As can clearly be seen, the peak stress (about 80 MPa) occurs right at the moment when the shock is applied (at 0.01 sec). After a fast damping pattern, a second peak is observed at 0.02 sec and the value of which is about 65 MPa. Severe impacts due to intermittent contact between the sensor plate and the base surface is seen from 0.01 sec till about 0.042 sec, which is indicated by the compressive stresses. After the period of the intermittent contacts, the plate is actually oscillating around a level which is slightly higher (towards +Z) from its neutral level. This behavior is also observed in Fig. 10 where the shock is in the -Z direction. It is revealed in Fig. 10 that this upward-moving oscillation is gradually going down and at

about 0.15 sec the oscillation is almost back around the neutral level with the stress amplitude close to zero. However, this pattern is not completely shown in Fig. 18, as the data get cut off at 0.125 sec due to excessive CPU time to solve the +Z case. It took a total CPU time of 288 hours of a SUN Ultra Sparc-10 workstation to get to 0.125 sec because of the highly nonlinear nature of the solutions [12]. Based on the -Z charts, we believe that after 0.125 sec all the results (stress, acceleration, velocity, etc) are of no importance as they are all practically approaching to zero. Thus, after 288 hours of CPU time, we decided to terminate the ABAQUS procedure. All the plots in the case of +Z, therefore, only show data till 0.125 sec.

Fig. 19 is the stress results near the tether in the center column, with the highest value being 200 MPa at the moment of initial impact. The behavior is again well expected, i.e., the highest peak at 0.01 sec and the second peak at 0.02 sec with no compressive stress due to downward motion restriction from the tether.

The nodal acceleration behavior is very different compared with the -Z case. Figs. 20 and 21 show the acceleration in the plate center and near the tether respectively. Unlike the acceleration behavior under the -Z shock, the acceleration under the +Z shock is around the neutral level of the sensor because the silicon base prevents further penetration. It is also seen that the acceleration near the tether is higher than that at the center of the sensor, which is also the case under -Z shock.

Figs. 22 and 23 present nodal velocity in these two locations of interest. There are no large spikes at 0.01 sec and 0.02 sec (as can be seen in the -Z case) mainly due to the intermittent contacts at the beginning of the shock. It is easy to see that the +Z shock produced nodal velocity that is well over an order of magnitude higher than that in the case of -Z shock.

The behavior of nodal displacement (Fig. 24 and 25) in these locations can be well conjectured. The lowest level the center point can move is -0.08 mil and instant contacts occurred at the time of shock application. After the shock duration, the

oscillation of the plate is around its neutral level and will eventually be damped to zero. The displacement near the tether exhibits an extremely similar pattern except the amplitudes are much smaller due to motion restriction from the tether.

7.4 Results of Dynamic Analysis in $\pm X$ Axis

Because of nearly symmetric geometry, dynamic analysis was performed only along the +X direction. As has been mentioned above, the locations of examination are no longer the same as that in Z-shock analysis since the center of the sensor is no longer a point of concern. Instead, we have identified the worst-case location being the edge of the sensor plate where it will have intermittent contact with the stopper under the shock along either +X or -X. In this section, we will examine three locations of interest, namely, the edge having contacts with the stopper, the point in close proximity to the tether in the center column (this is also the location examined in the $\pm Z$ analyses), and the tip of the sensor finger (attached to the sensor plate) in the center column. For each variable to be discussed below, these three locations will be shown in that order for simplicity. To save CPU time without losing critical information, the analysis was conducted for the length of 0.1 sec.

The worst-case stress among all the cases analyzed in this study, as intuitively conjectured, is at the edge having contact with the stopper. The time history of the maximum principal stress is depicted in Fig. 26. As can be seen, the highest impact stress is as high as 450 MPa, which is induced by the initial contacts. Within the duration of the shock, the stress magnitude decreases fairly rapidly due to the damping effect. It is interesting to note that the time duration of higher stress (above 150 MPa in Fig. 26) lasts longer than the duration of the shock (0.01 sec total time). Recalling the -Z shock analysis where there are intermittent contacts, the typical duration of higher stress is almost identical to the duration of the shock, which is from 0.01 sec to 0.02 sec (see Fig. 10). In the case of +Z analysis, however, the higher stress duration is also lasting longer than the duration of the shock (see Fig. 18). It is obvious that motions shown in Fig. 18

and Fig. 26 have much severer intermittent contacts than that shown in Fig. 10. There is no doubt that the higher stress duration in Fig. 26 must be at most equal to or even less than the duration of intermittent contact because, if without contact, a mere 1.2 μm maximum displacement (1.2 μm being the gap between the stopper and the edge of the center plate) cannot possibly induce such high stresses. Similar arguments can also be made directly to the stress behavior in Fig. 18 where the gap underneath the center plate is only 2 μm . Nevertheless, even the stress behavior in Fig. 18 is somewhat similar to that in Fig. 26, the dynamic impact due to intermittent contacts is far severer in Fig. 26 as the relative stress level (compared to the respective peak stress) within the higher stress duration is much higher. This is because the intermittent contacts are double-sided in X-shock scenario since both edges of the sensor are restricted in movement by the stoppers. Thus, the frequency of impact is much higher and the higher stress duration is relatively longer.

A slightly different stress pattern is found at the point in close proximity to the tether in the center column (Fig. 27). It is quite clear that the duration of higher stress is practically no longer than the duration of the input shock simply because there are no contacts in this area of the sensor. The highest stress at this point is just above 300 MPa. In Z analysis, the stress in this location is the highest in the whole sensor, but in the X shock scenario, the highest stress is actually at the center of the edge contacting with the stopper. This conclusion is physically reasonable because, in $\pm Z$ shock, the contact area between the sensor plate and the silicon base is as large as the whole area of the center plate. In the X shock, the area of intermittent contact is equal only to the area of the vertical surface (facing the center of the sensor) of the stopper head (see Fig. 9). It is this small and rigid area (roughly 40 μm^2) that takes the dynamic impact load directly from the center plate of the sensor.

The last area of interest in this +X analysis is the tip of the sensor finger in the center column, and its stress behavior is plotted in Fig. 28. Again, because of the double-sided intermittent contact, the duration of higher stress is longer than the duration of shock input. The highest stress is less than 80 MPa. The mild stress is likely to be

caused by the deform-deform intermittent contact because deformation of the contact surfaces of the moving fingers allows more traveling distances between the contacts and therefore, reduces the intensity of structural impact.

Since the center point of the edge of the sensor has been determined to be the worst-case location in terms of high stresses, we will only present results of interest in this particular location. Fig. 29 is the nodal acceleration at this edge point where the dominant acceleration is induced by the initial intermittent contacts. The magnitude of acceleration decreases quickly, indicating fast consumption of kinetic energy due to high-frequency intermittent contacts. The displacement history at the center of the edge is shown in Fig. 30, where it clearly indicates the spacing restriction of nodal traveling imposed by the stoppers at each end of the sensor plate. It can also be deduced from Fig. 30 that the time duration of intermittent contacts starts at 0.01 sec and ends at about 0.028 sec, lasting 0.018 sec of time. This also provides further explanation to the longer “duration of higher stress” observed in Fig. 26 and Fig. 28.

Examining all the results of the maximum principal stress has lead us to conclude that the microsensor structure of this accelerometer shall not fail due to brittle fracture of thin-film silicon under pulsed 2000g shock in all the three axes. This prediction will hold even if we utilize the most conservative criterion, namely, 0.6 GPa fracture strength. This conclusion supports the manufacturer’s maximum rating for the device, and is also verified by the NASA experiment in which the accelerometer was subject to 2000g shocks in its three axes [13].

8. CONCLUSIONS

Using the nonlinear direct dynamic integration techniques together with sophisticated mathematical treatment of high-frequency impact resulting from intermittent contact, we have obtained a good insight of the dynamic performance of this MEMS accelerometer under 2000g pulsed shock conditions. Based on a series of modal

analysis, this assessment also provided more practical information as guidelines for the proper mounting of the device when preparing for the actual measurements. A properly mounted device must have the correct sensing orientation and the required dynamic stiffness to avoid spurious signal output. When the system configuration is complex, an in-depth dynamic study will be required for a proper mounting.

The dynamic response results obtained under 2000g shock conditions indicate that the maximum acceleration rating of this device (2000g) is acceptable. A 2000g pulsed shock applied in the normal sensing orientation resulted in a 0.45 GPa peak stress, which is concentrated at the edge of the proof mass plate as the consequence of high-frequency intermittent contacts with the head of the stopper. The stresses are significantly lower if the shock is applied in the direction perpendicular to the sensing direction despite the fact that severe intermittent contacts also occur. Shocks in the perpendicular direction can usually be avoided by the proper mounting of the device in most commercial applications, but in space flight applications it is by no means easily avoidable. The results of the analysis provide that if the device can withstand a given shock in its sensing orientation, it should have no problem surviving the same shock in the direction perpendicular to the sensing axis. This analytical result has practically removed the need for multi-axis dynamic testing, if it is planned based on generic requirements.

Although 0.45 GPa does provide a sense of safety at 2000g, it is by no means adequate to deploy the device in such a harsh dynamic environment from the material perspective. Since brittle fracture strength of thin-film silicon is highly surface-roughness dependent, a film with a rougher-than-usual backside used in the device fabrication could have a lower fracture strength and could fracture under 2000g. For almost all the fracture strength testing reported, the films were carefully selected and prepared to weed out the rougher-than-usual specimens. Thus, the 0.60 GPa fracture strength, although considered very conservative, was derived from samples without abnormal roughness. Taking into consideration the possibility of thin-film material variation during the device fabrication process, we recommend the use of this device for

NASA missions under the nominal temperature range with a maximum acceleration limit of 1500g.

The second phase of this assessment will deal with the dynamic characteristics of the device under the cryogenic conditions.

REFERENCES

- [1] “ $\pm 5g$ to $\pm 50g$, low noise, low power, single/dual axis iMEMS accelerometers”, *Analog Device, Inc. document*, Rev. 0, 1998.
- [2] Ericson, F. and Schweitz, J-A., “Micromechanical fracture strength of silicon”, *J. Appl. Phys.*, Vol. 68, No. 11, pp. 5840-5844, 1990.
- [3] Johansson, S. and Schweitz, J-A., “Fracture testing of silicon microelements *in situ* in a scanning electron microscope”, *J. Appl. Phys.*, Vol. 63, No. 10, pp. 4799-4803, 1988.
- [4] Wilson, C. J., Ormeggi, A., and Narbutovskih, M., “Fracture testing of silicon microcantilever beams”, *J. Appl. Phys.*, Vol. 79, No. 5, 1996.
- [5] Saif, M. T. A. and MacDonald, N. C., “Measurement of forces and spring constants of microinstruments”, *Rev. Sci. Instrum.*, Vol. 69, No. 3, 1998.
- [6] Zhoga, L. V., Kozachuk, A. I., Stepanov, V. A., Tutovets, Y. F., and Shpeizman, V. V., “Brittle strength of Si single crystals and its relationship to the lifetime under static and cyclic loads”, *Sov. Phys. Solid State*, Vol. 21, No. 11, 1979.
- [7] Hilber, H. M., Hughes, T. J. R., and Taylor, R. L., “Collocation, dissipation and ‘overshoot’ for time integration schemes in structural dynamics”, *Earthquake Eng. Struct. Dynamics*, Vol. 6, pp. 99-117, 1978.
- [8] Hibbitt, H. D. and Karlsson, B. I., “Analysis of pipe whip”, *EPRI, Report NP-1208*, 1979.

[9] This is true for most of the elements in ABAQUS, but several beam elements do not follow this rule. The FEA model established for the current work does not use those beam elements.

[10] Shuster, M, Briano, B, and Kitchin, C., “Increasing the frequency response of the ADXL series accelerometers”, *Analog Device, Inc. Application Note AN-377*.

[11] This is true in the initial oscillating motions when the effect of impact is the severest. The motion of the force fingers and the sensor fingers could go out of phase after perhaps several initial impacts. However, the stresses induced by impact decrease fairly rapidly due to the intrinsic damping. Thus the focus of analysis is on the moment of initial impact when the stress is the highest.

[12] During the intermittent contact time period from 0.01 sec to nearly 0.05 sec, ABAQUS’ averaged iterative time increment was as small as 2×10^{-6} . In fact, several increments at the initial contact time (at 0.01 sec) were as tiny as 1×10^{-9} .

[13] Teverovsky, A. and Sharma, A., “Evaluation of thermal-mechanical stability of COTS dual-axis MEMS accelerometers for Space Applications,” *NASA NEPP Report*, April 2000.

LIST OF ILLUSTRATIONS

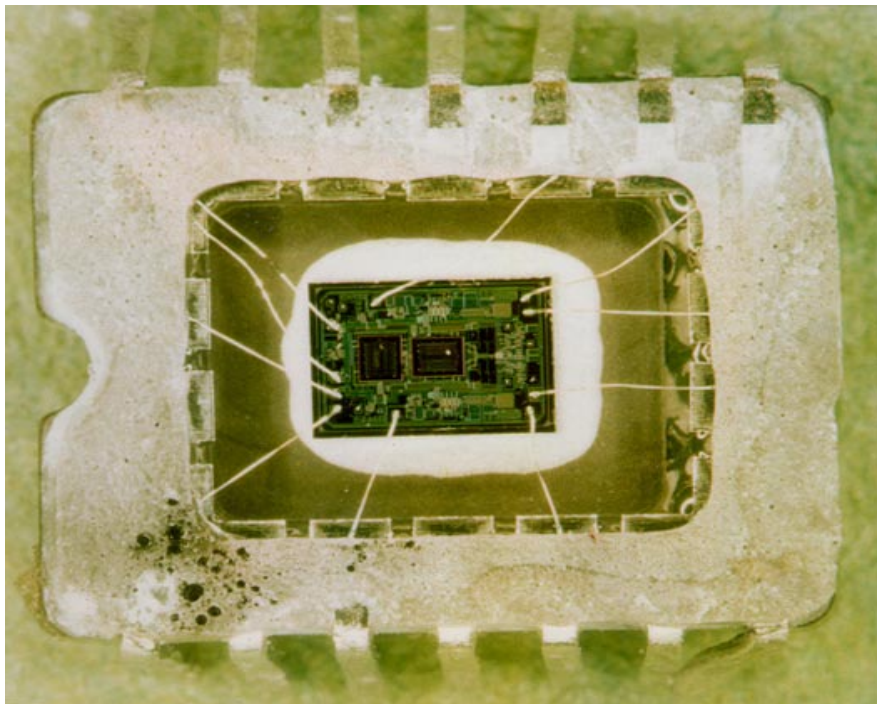


Fig. 1 ADXL250 accelerometer device with the lid removed

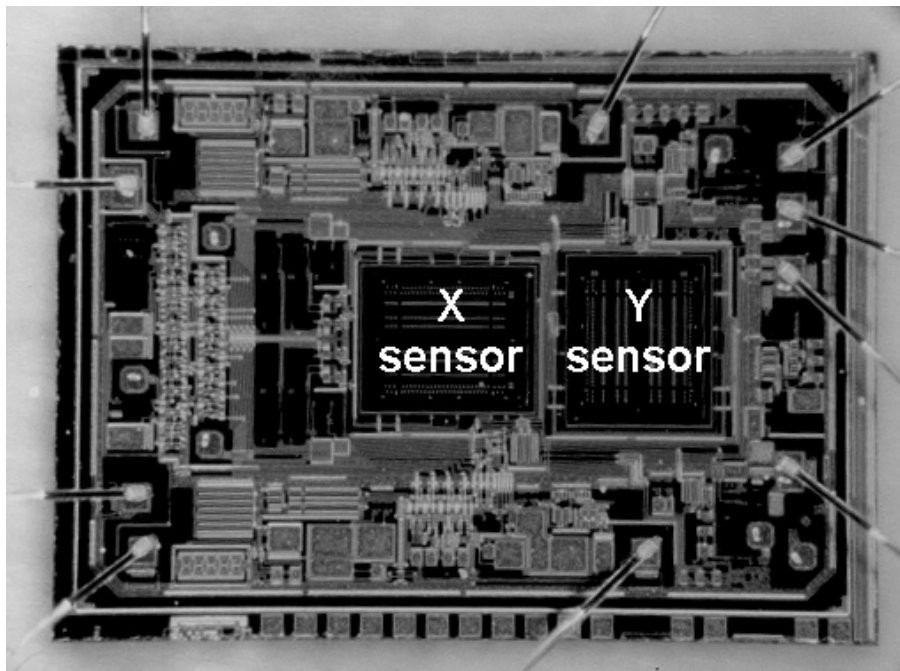


Fig. 2 Overall layout of the sensor elements

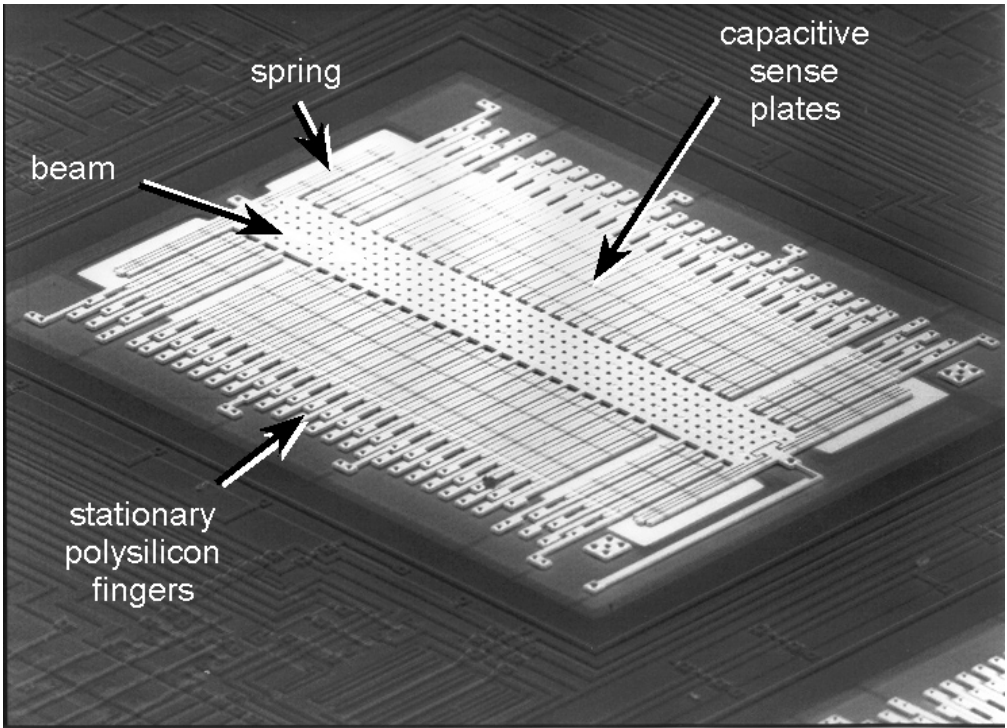


Fig. 3 Enlarged view of one of the sensors

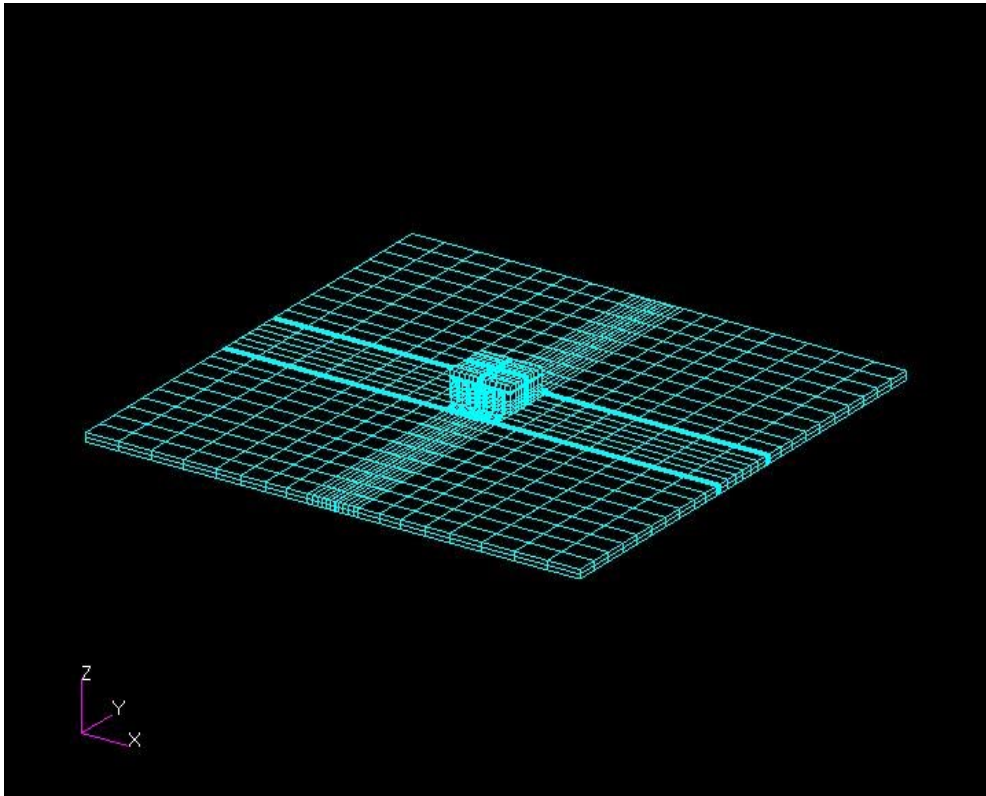


Fig. 4 Overall 3-D FEA model

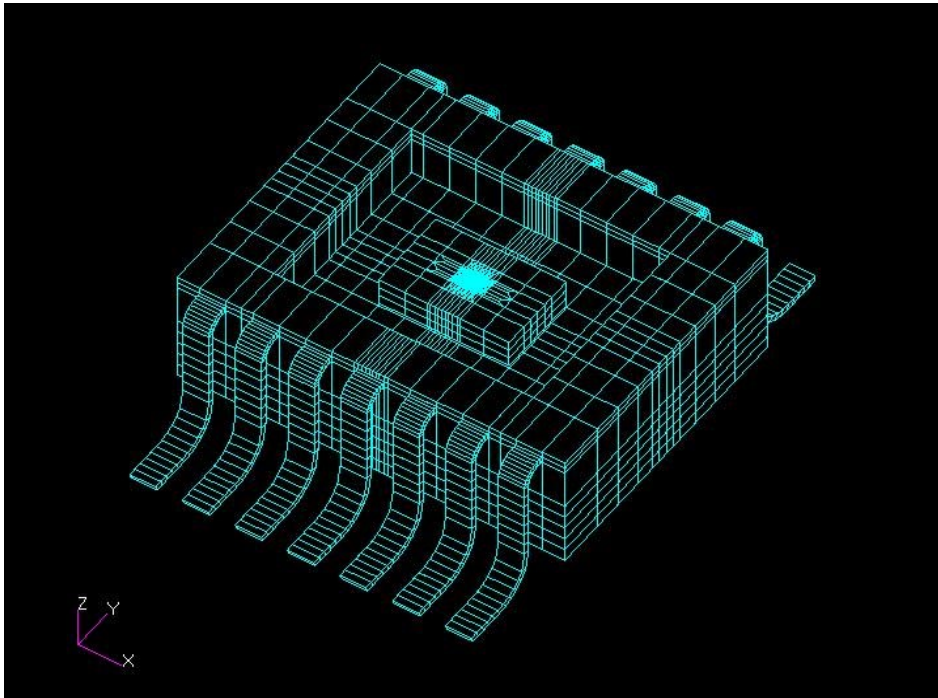


Fig. 5 Enlarged device model with the lid removed

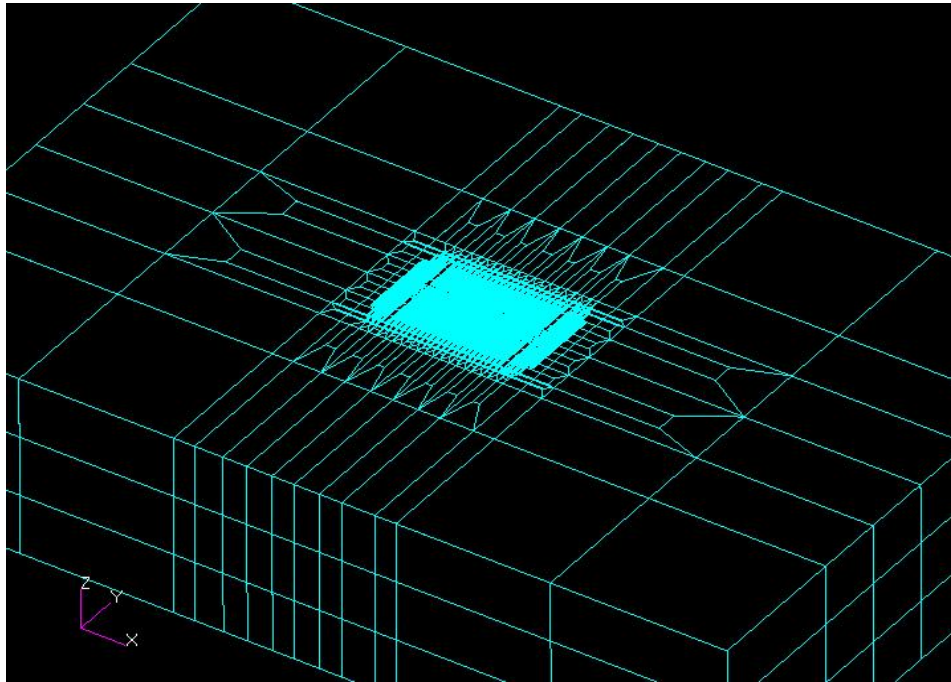


Fig. 6 Enlarged FEA model for the sensor area

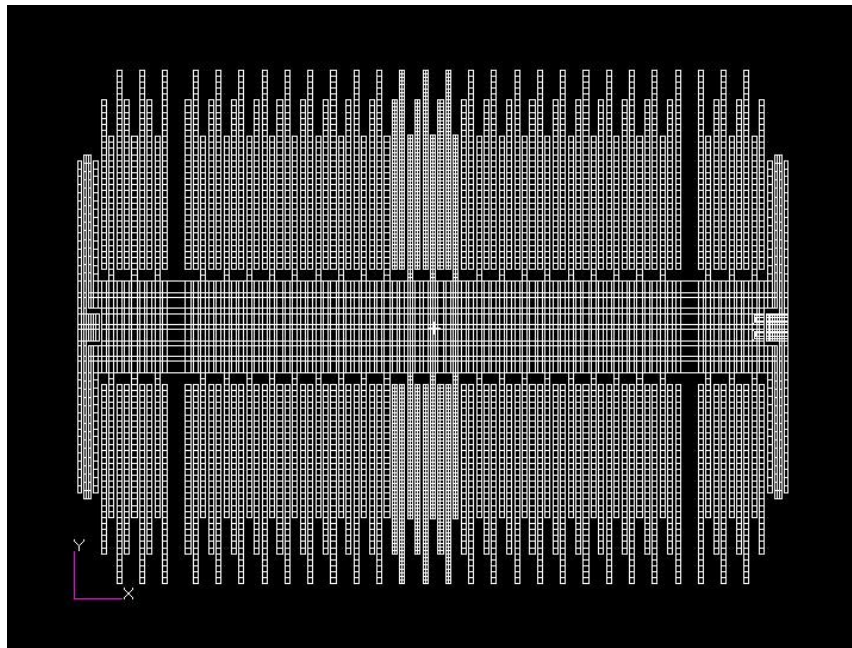


Fig. 7 Details of the FEA model for the sensor (top view)

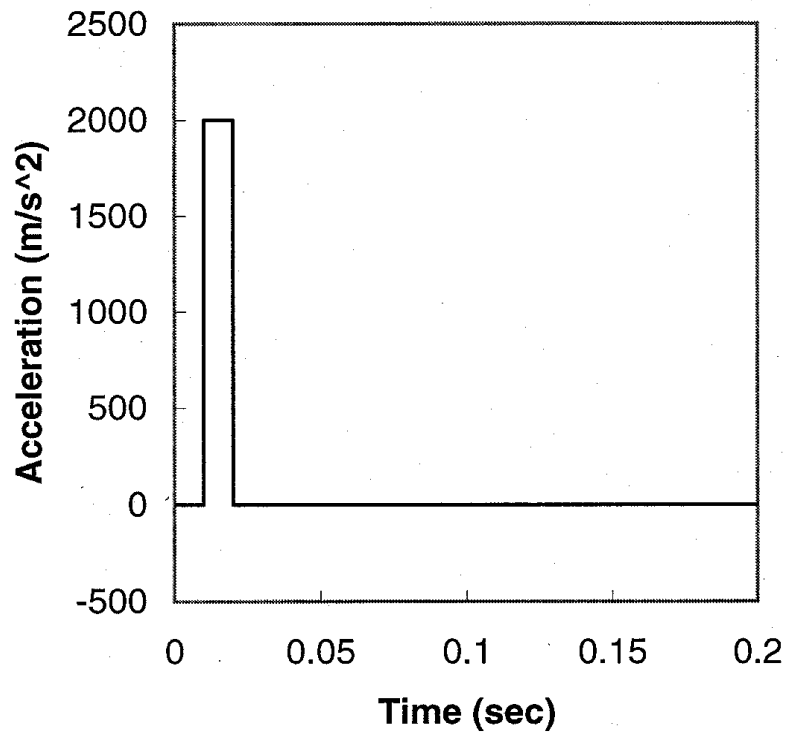


Fig. 8 Input shock

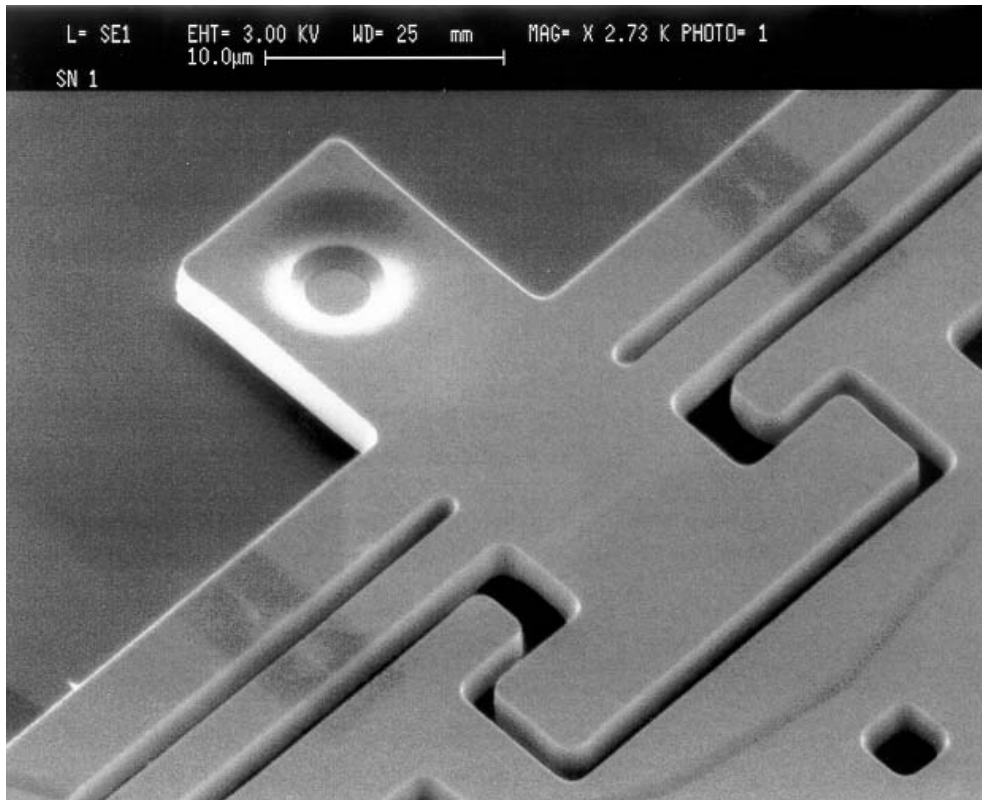


Fig. 9 Motion stopper structure

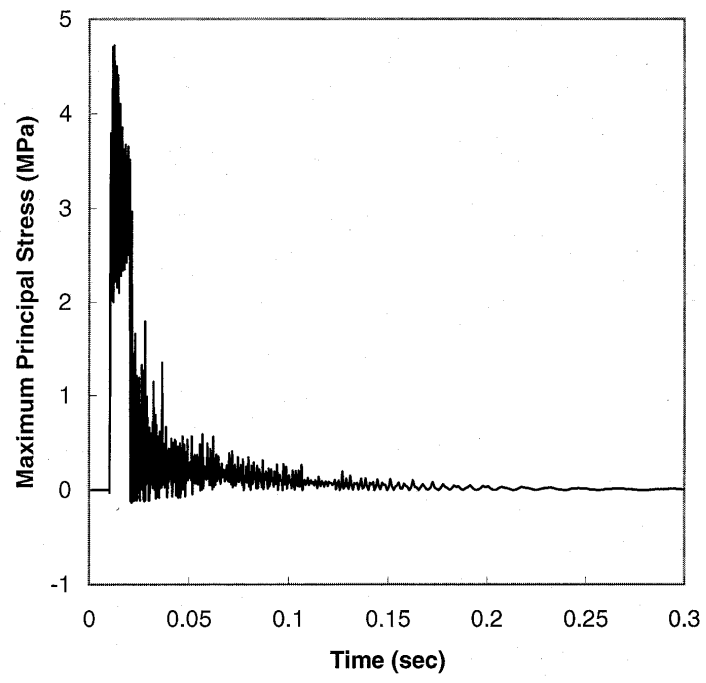


Fig. 10 Maximum principal stress at the center of the center plate ($-Z$ shock)

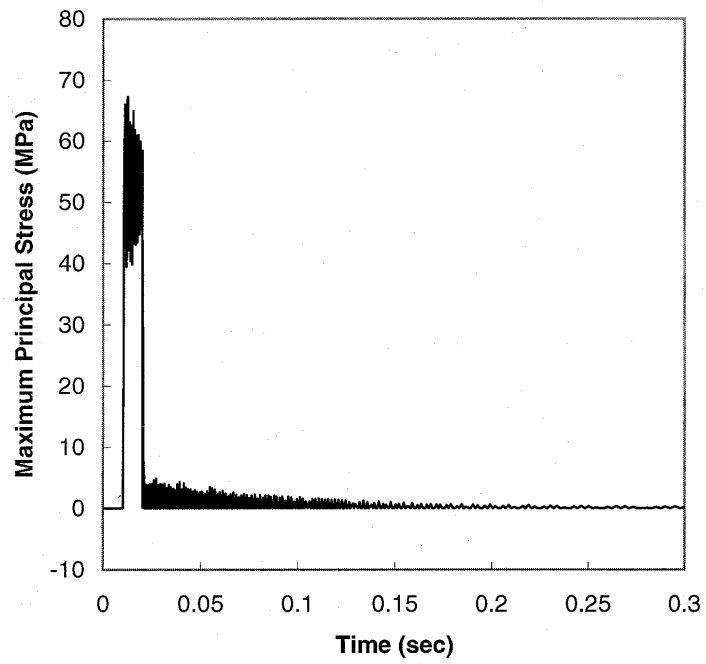


Fig. 11 Maximum principal stress in the center column tether area (-Z shock)

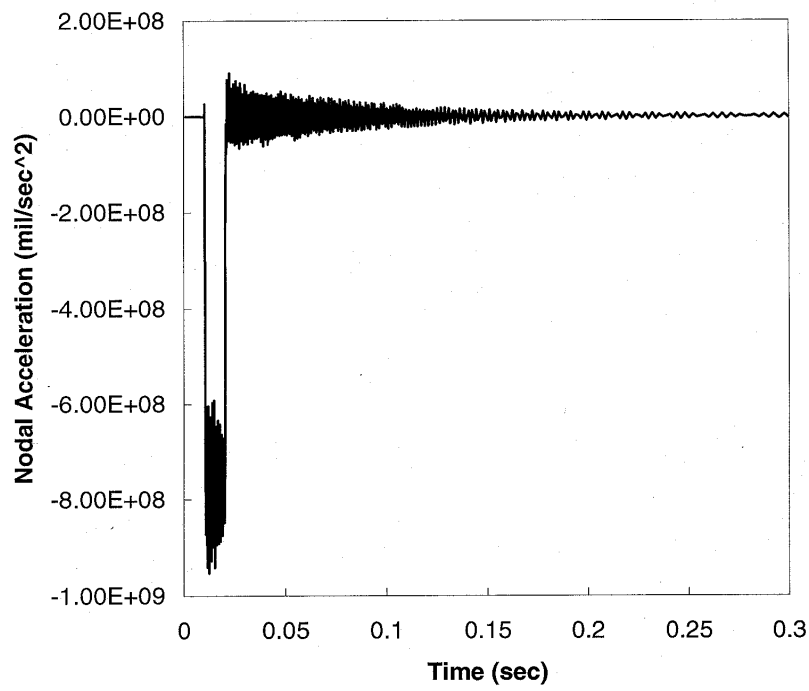


Fig. 12 Nodal acceleration at the center of the center plate ($-Z$ shock)

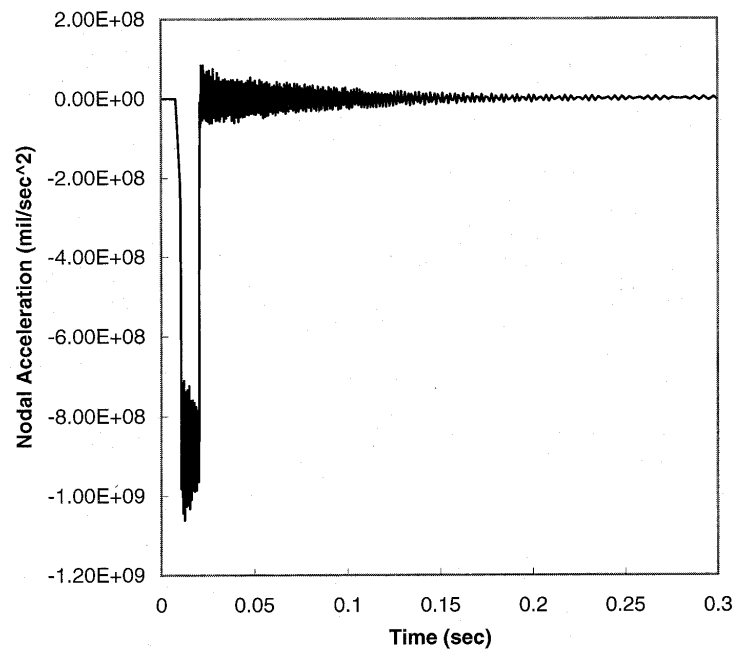


Fig. 13 Nodal acceleration in the center column tether area (-Z shock)

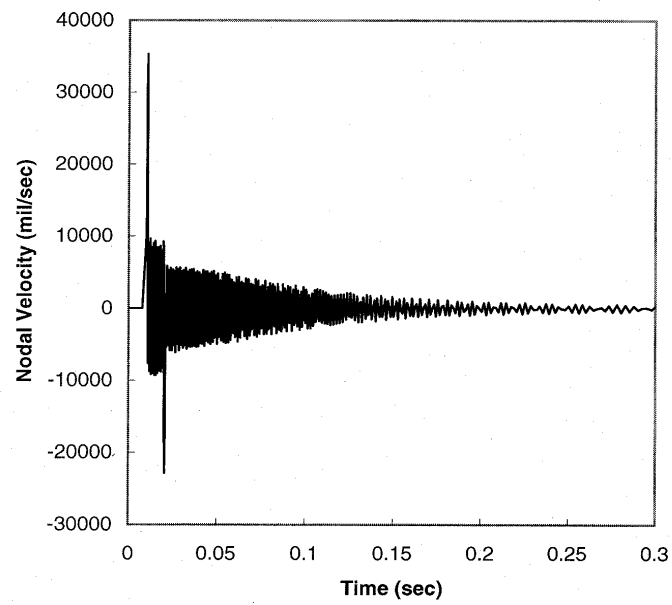


Fig. 14 Nodal velocity at the center of the center plate (-Z shock)

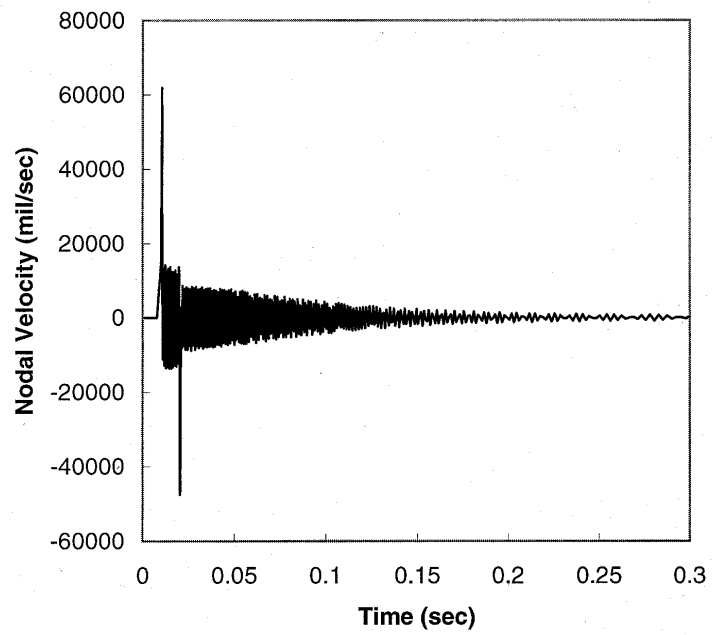


Fig. 15 Nodal velocity in the center column tether area ($-Z$ shock)

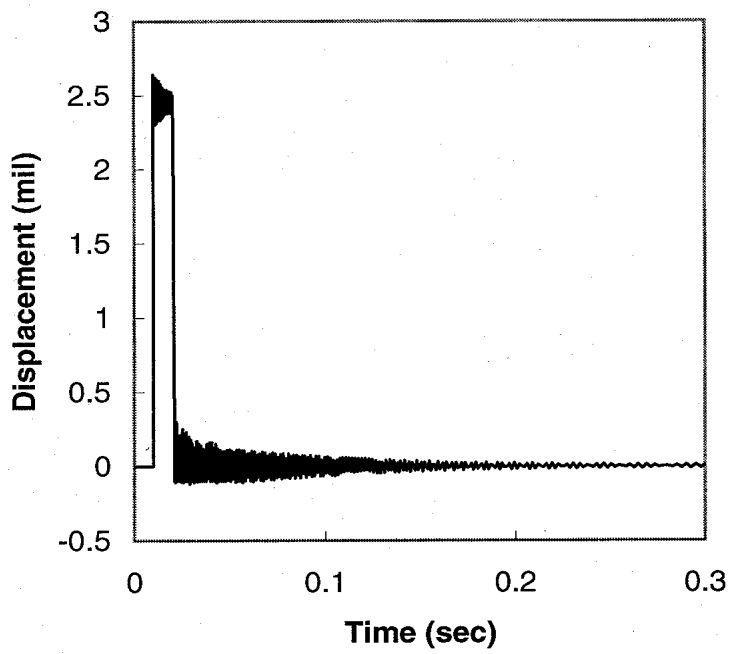


Fig. 16 Nodal displacement at the center of the center plate (-Z shock)

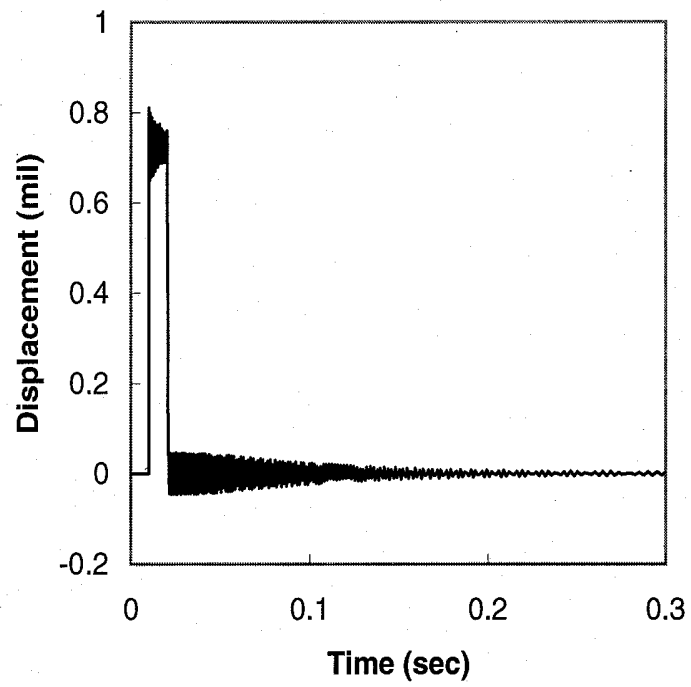


Fig. 17 Nodal displacement in the center column tether area (-Z shock)

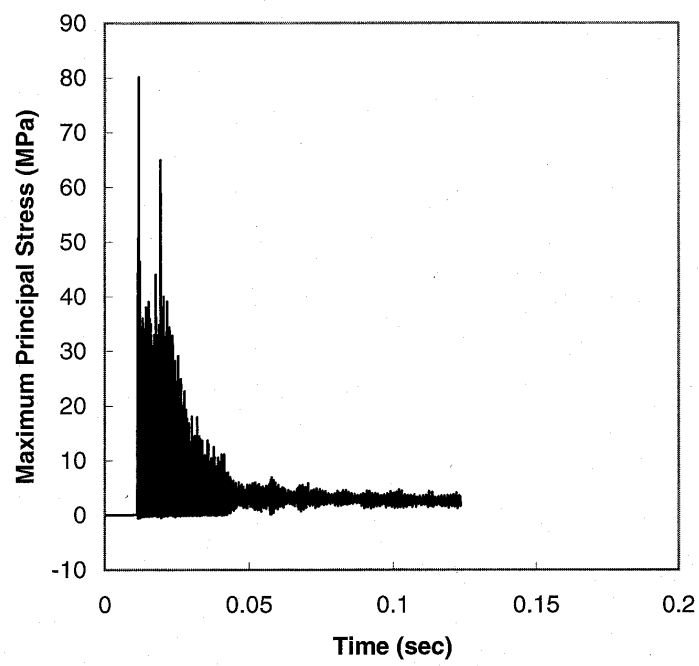


Fig. 18 Maximum principal stress at the center of the center plate (+Z shock)

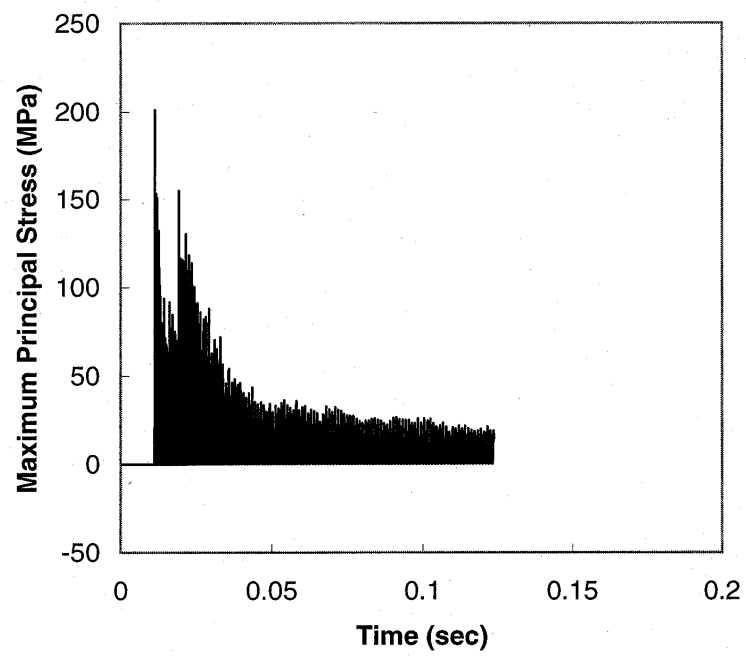


Fig. 19 Maximum principal stress in the center column tether area (+Z shock)

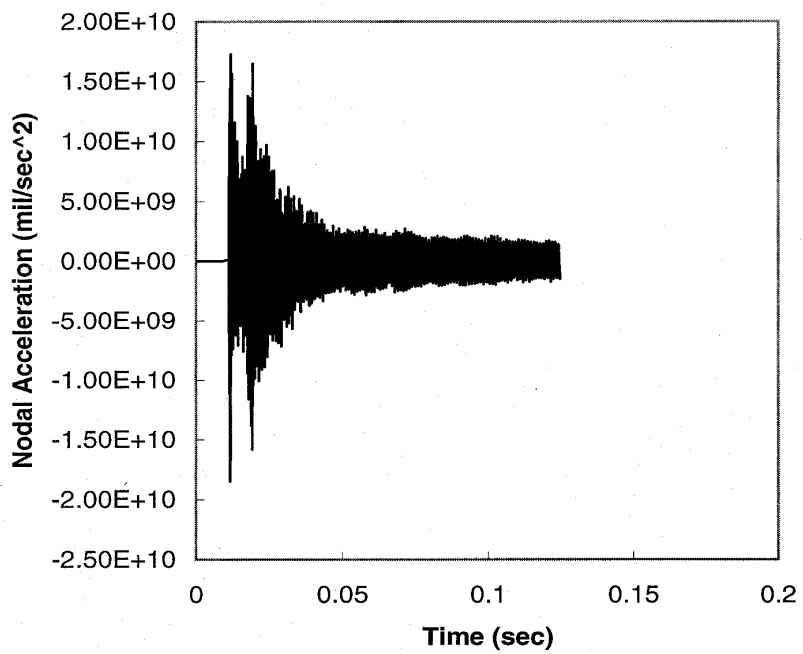


Fig. 20 Nodal acceleration at the center of the center plate (+Z shock)

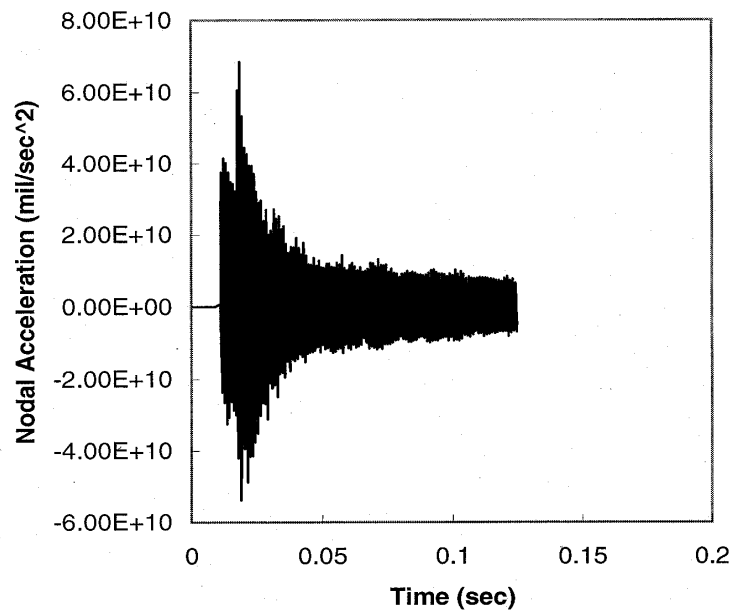


Fig. 21 Nodal acceleration in the center column tether area (+Z shock)

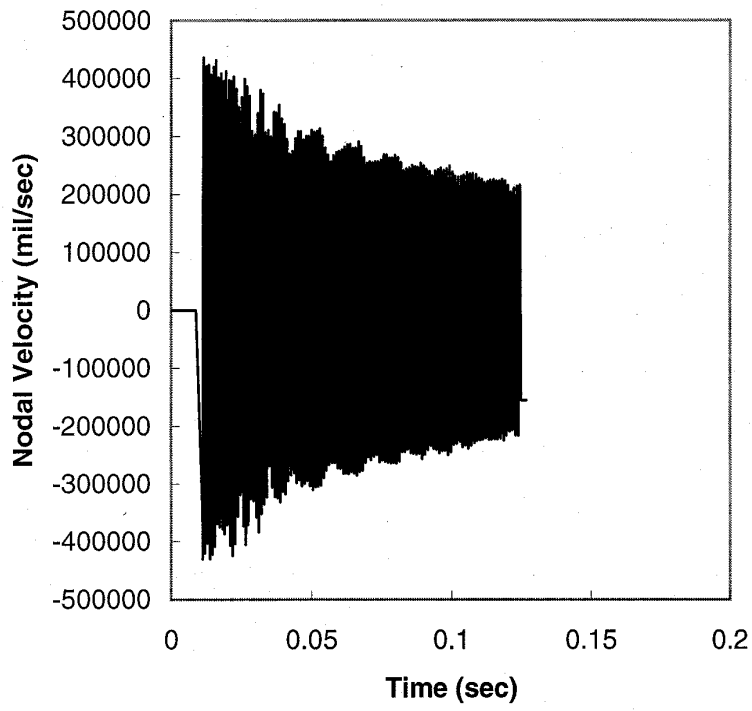


Fig. 22 Nodal velocity at the center of the center plate (+Z shock)

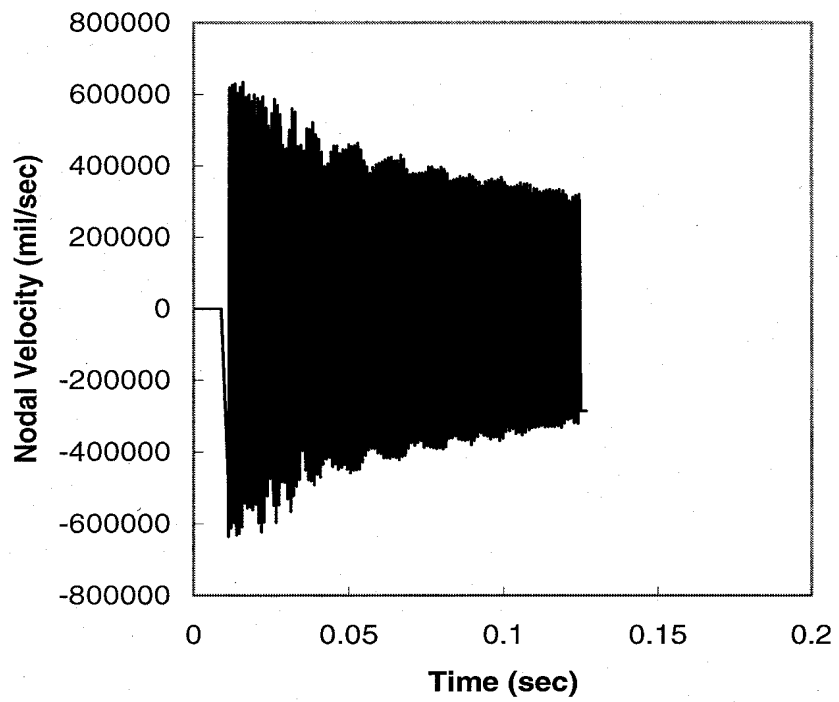


Fig. 23 Nodal velocity in the center column tether area (+Z shock)

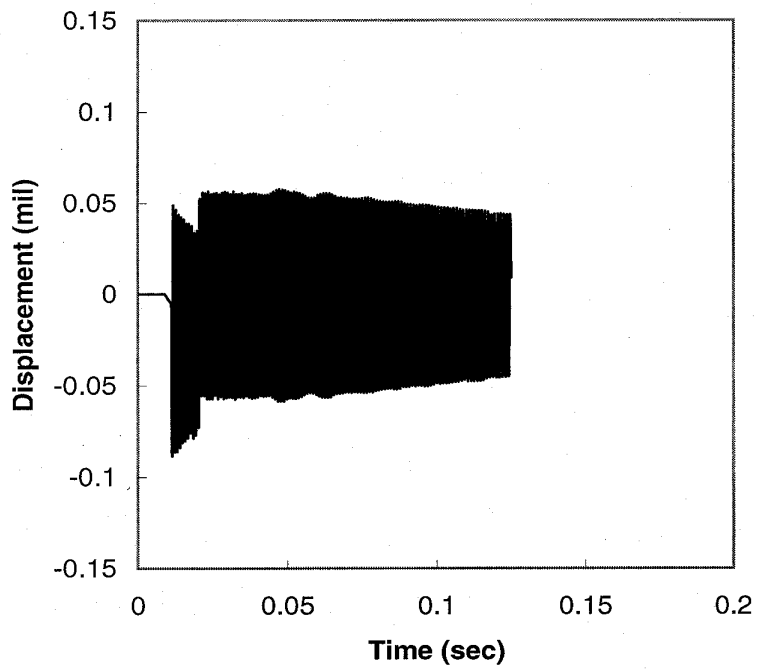


Fig. 24 Nodal displacement at the center of the center plate (+Z shock)

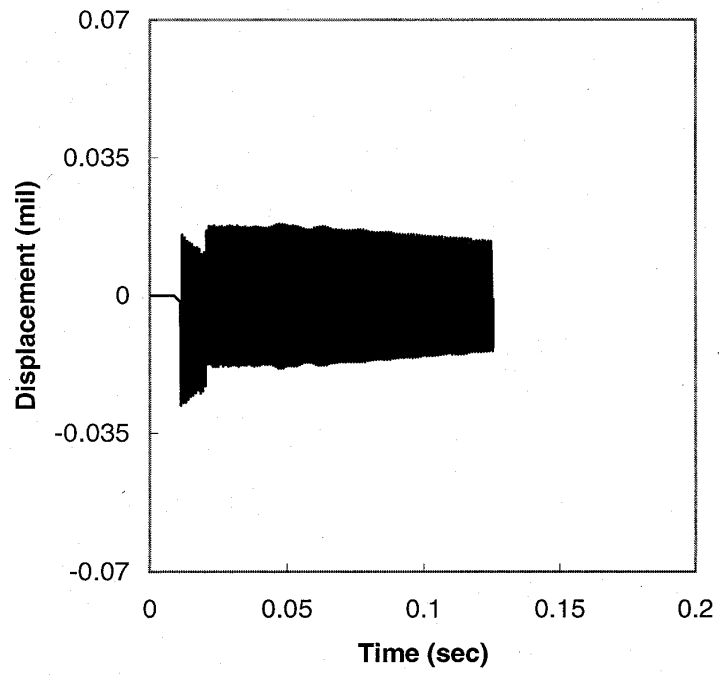


Fig. 25 Nodal displacement in the center column tether area (+Z shock)

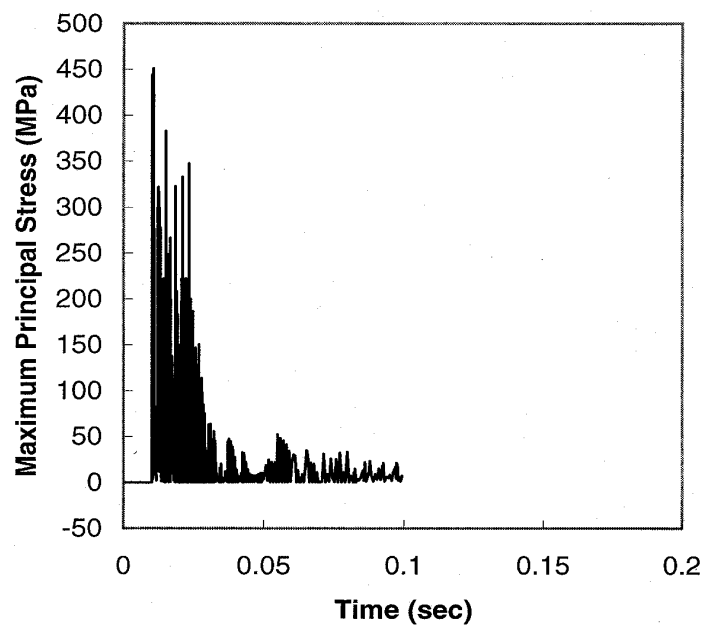


Fig. 26 Maximum principal stress at the edge of the sensor (X shock)

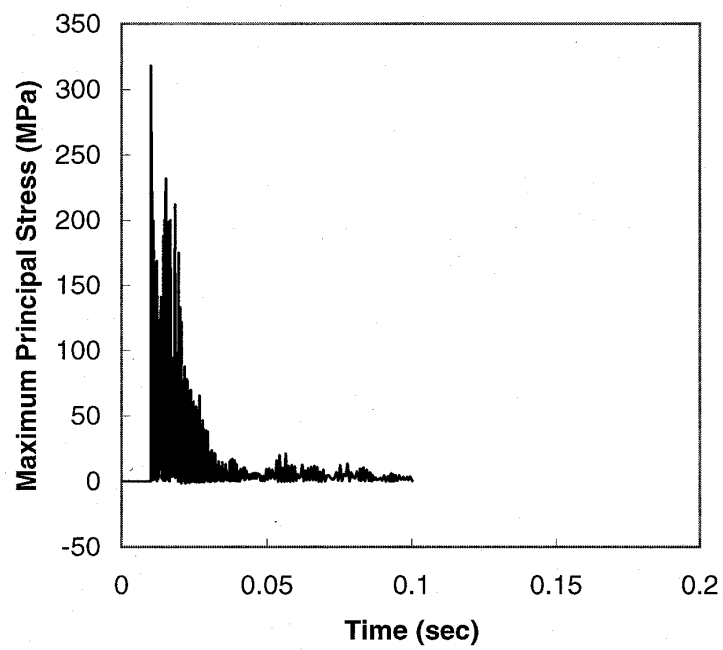


Fig. 27 Maximum principal stress in the center column tether area (X shock)

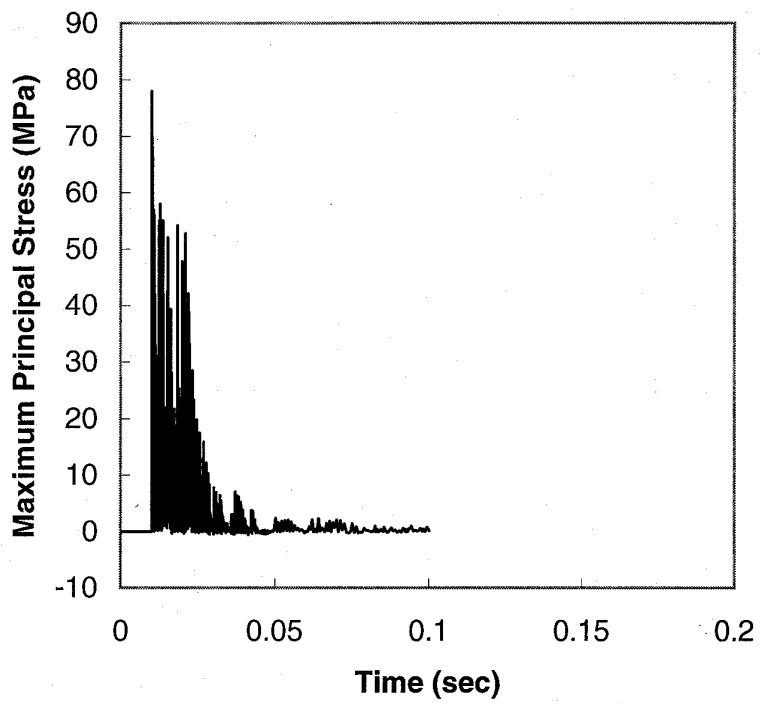


Fig. 28 Maximum principal stress at the tip of the sensor finger in the center column (X shock)

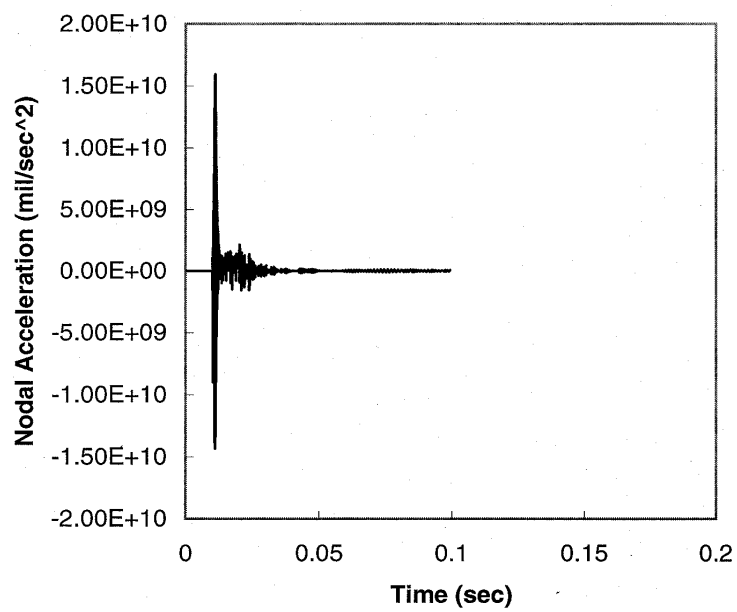


Fig. 29 Nodal acceleration at the edge of the sensor (X shock)

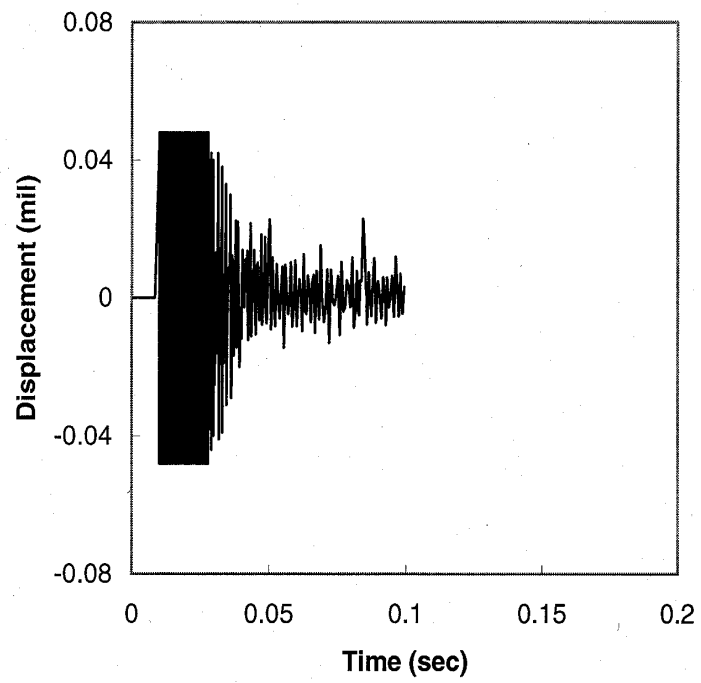


Fig. 30 Nodal displacement at the edge of the sensor (X shock)

REPORT DOCUMENTATION PAGE

Form Approved
OMB No. 0704-0188

Public reporting burden for this collection of information is estimated to average 1 hour per response, including the time for reviewing instructions, searching existing data sources, gathering and maintaining the data needed, and completing and reviewing the collection of information. Send comments regarding this burden estimate or any other aspect of this collection of information, including suggestions for reducing this burden, to Washington Headquarters Services, Directorate for Information Operations and Reports, 1215 Jefferson Davis Highway, Suite 1204, Arlington, VA 22202-4302, and to the Office of Management and Budget, Paperwork Reduction Project (0704-0188), Washington, DC 20503.

1. AGENCY USE ONLY (<i>Leave blank</i>)		2. REPORT DATE October 2001	3. REPORT TYPE AND DATES COVERED Technical Paper	
4. TITLE AND SUBTITLE Dynamic Response Assessment for the MEMS Accelerometer Under Severe Shock Loads			5. FUNDING NUMBERS 562	
6. AUTHOR(S) Mark S. Fan and Harry C. Shaw				
7. PERFORMING ORGANIZATION NAME(S) AND ADDRESS (ES) Goddard Space Flight Center Greenbelt, Maryland 20771			8. PERFORMING ORGANIZATION REPORT NUMBER 2002-01008-0	
9. SPONSORING / MONITORING AGENCY NAME(S) AND ADDRESS (ES) National Aeronautics and Space Administration Washington, DC 20546-0001			10. SPONSORING / MONITORING AGENCY REPORT NUMBER TP—2001—209978	
11. SUPPLEMENTARY NOTES				
12a. DISTRIBUTION / AVAILABILITY STATEMENT Unclassified—Unlimited Subject Category: 39 Report available from the NASA Center for AeroSpace Information, 7121 Standard Drive, Hanover, MD 21076-1320. (301) 621-0390.			12b. DISTRIBUTION CODE	
13. ABSTRACT (<i>Maximum 200 words</i>) NASA Goddard Space Flight Center (GSFC) has evaluated the dynamic response of a commercial-off-the-shelf (COTS) MEMS device made by Analog Device, Inc. The device is designated as ADXL250 and is designed mainly for sensing dynamic acceleration. It is also used to measure the tilting angle of any system or component from its original level position. The device has been in commercial use (e.g., in automobile airbag deployment system as a dual-axial accelerometer and in the electronic game play-station as a tilting sensor) with success, but NASA needs an in-depth assessment of its performance under severe dynamic shock environments. It was realized while planning this evaluation task that two assessments would be beneficial to NASA's missions: 1. severe dynamic shock response under nominal thermal environments and 2. general dynamic performance under cryogenic environments. The first evaluation aims at obtaining a good understanding of its micromachined structure within a framework of brittle fracture dynamics, while the second evaluation focuses on the structure integrity under cryogenic temperature conditions. The information we gathered from the manufacturer indicated that the environmental stresses under NASA's evaluation program have been far beyond what the device has experienced with commercial applications, for which the device was designed [1]. Thus NASA needs the outcome of this evaluation in order to make the selection for possible use for its missions. This paper provides details of the first evaluation—the dynamic response under severe multi-axial single-pulse shock load. It was performed using finite element tools with nonlinear dynamics procedures.				
14. SUBJECT TERMS MEMS accelerometer, dynamic acceleration, tilting angle sensor.			15. NUMBER OF PAGES 64	
			16. PRICE CODE	
17. SECURITY CLASSIFICATION OF REPORT Unclassified	18. SECURITY CLASSIFICATION OF THIS PAGE Unclassified	19. SECURITY CLASSIFICATION OF ABSTRACT Unclassified	20. LIMITATION OF ABSTRACT UL	